

Globally Divergence-Free Discontinuous Galerkin Methods for Ideal Magnetohydrodynamic Equations

Pei Fu¹ · Fengyan Li² · Yan Xu¹ 

Received: 3 October 2017 / Revised: 5 April 2018 / Accepted: 29 May 2018 / Published online: 8 June 2018
© Springer Science+Business Media, LLC, part of Springer Nature 2018

Abstract Ideal magnetohydrodynamic (MHD) equations are widely used in many areas in physics and engineering, and these equations have a divergence-free constraint on the magnetic field. In this paper, we propose high order globally divergence-free numerical methods to solve the ideal MHD equations. The algorithms are based on discontinuous Galerkin methods in space. The induction equation is discretized separately to approximate the normal components of the magnetic field on elements interfaces, and to extract additional information about the magnetic field when higher order accuracy is desired. This is then followed by an element by element reconstruction to obtain the globally divergence-free magnetic field. In time, strong-stability-preserving Runge–Kutta methods are applied. In consideration of accuracy and stability of the methods, a careful investigation is carried out, both numerically and analytically, to study the choices of the numerical fluxes associated with the electric field at element interfaces and vertices. The resulting methods are local and the approximated magnetic fields are globally divergence-free. Numerical examples are presented to demonstrate the accuracy and robustness of the methods.

Keywords MHD equations · Divergence-free magnetic field · Discontinuous Galerkin methods · $H(\text{div})$ -conforming finite element spaces · Fourier analysis

Research of F. Li is supported in part by NSF Grants DMS-1318409 and DMS-1719942. Research of Y. Xu is supported by NSFC Grant Nos. 11722112 and 91630207.

✉ Yan Xu
yxu@ustc.edu.cn

Pei Fu
sxfp2013@mail.ustc.edu.cn

Fengyan Li
lif@rpi.edu

¹ School of Mathematical Sciences, University of Science and Technology of China, Hefei 230026, Anhui, China

² Department of Mathematical Sciences, Rensselaer Polytechnic Institute, Troy, NY 12180, USA

1 Introduction

In this paper, we will develop globally divergence-free discontinuous Galerkin (DG) methods to numerically simulate ideal magnetohydrodynamic (MHD) equations. MHD equations model ionized plasmas under some simplified assumptions and are widely used for describing many problems in physics and engineering. The ideal MHD equations considered in this work can be written as a system of nonlinear hyperbolic conservation laws, in addition to a divergence-free constraint on the magnetic field. Even though the magnetic field in the exact solution satisfies the divergence-free condition as long as it does initially, insufficient preservation of this property numerically may lead to numerical instability or nonphysical features of approximated solutions [8, 9, 19, 37].

To handle the divergence-free constraint, various strategies have been developed in numerical modeling and mathematical analysis within divergence-cleaning or divergence-free algorithms. In [9], Brackbill and Barnes proposed a simple divergence correction technique based on Hodge decomposition. They projected the computed magnetic field into a divergence-free vector space by solving a Poisson equation and used the divergence-free magnetic field in the next time step. One widely used framework to achieve the preservation of the divergence, in some discrete or continuous sense, is “constrained transport”, introduced by Yee [40] in the context of the electromagnetism, and adapted by Evans and Hawley [19] to MHD simulations. This idea was further developed by many researchers within frameworks of finite difference, finite volume, and finite element methods, either upwind (also called Godunov) or central types, and with various accuracy [8, 17, 20, 26, 29]. Among the developments, there are exactly divergence-free numerical methods [1, 3, 26, 28, 29, 35]. Other approaches which attract different practitioners include Powell’s source term formulation [30] by adding source terms depending on $\nabla \cdot \mathbf{B}$, and generalized multiplier methods [18] with divergence cleaning technique.

In recent years, Li et al. [25–27, 38] developed divergence-free numerical methods for ideal MHD equations based on DG and central DG spatial discretizations. In [25], locally divergence-free DG methods were formulated, and they utilize divergence-free vector spaces inside each mesh element to approximate the magnetic field. In [26, 27], exactly divergence-free central DG methods were proposed for ideal MHD equations, and the methods can be of arbitrary accuracy. The discrete space to represent and to compute the magnetic field is a divergence-free subspace of the Brezzi–Douglas–Marini (BDM) finite element space [10], a well-established $H(\text{div})$ -conforming finite element space. DG method was first introduced in 1973 by Reed and Hill for linear neutron transport problems [33]. A major breakthrough was made by Cockburn et al. [13–16] to develop DG spatial discretizations for nonlinear hyperbolic conservation laws, coupled with high order Runge–Kutta methods in time. Exact or approximate Riemann solvers are used as numerical fluxes at element interfaces, and total variation bounded (TVB) nonlinear limiters [36] are applied in the presence of strong shocks to achieve non-oscillatory property. With their great flexibility in local approximations and geometry, local conservation, and high parallel efficiency, DG methods since then have been formulated and analyzed to various mathematical models, with broad applications in areas such as electromagnetism, gas dynamics, granular flow, plasma physics etc. One can refer to [22, 24, 34] for a more systematic description of the methods as well as their implementation and applications.

Our present work follows the development of exactly divergence-free central DG methods for ideal MHD equations in [26, 27], and it is related to the exactly divergence-free DG methods for the induction equation using multi-dimensional Riemann solvers [7]. On the one

hand, the methods in [26,27] achieve exactly divergence-free approximations for the magnetic field within a relatively simple formulation due to that the methods involve two copies of numerical solutions from two overlapping meshes, and no numerical fluxes are needed either on element interfaces or at mesh vertices. On the other hand, two copies of numerical solutions double the total number of unknowns and hence increase the computational complexity of the algorithms. In this work, we want to design exactly divergence-free DG methods that are defined on one mesh, which is structured, for ideal MHD equations in two dimensions. Similar as in central DG framework, our new methods will discretize the hydrodynamic variables, such as density, momentum, total energy using standard DG methods, while the equations evolving the magnetic fields, referred to as the induction equation, will be discretized differently by DG-type methods. More specifically, the normal components of the magnetic field along element edges will be updated first by DG methods defined on edges, and this is followed by an element-wise reconstruction to produce an exactly divergence-free magnetic field. For higher order accuracy, additional information will be computed for the magnetic field, and it will be used together with the normal components of the magnetic field to uniquely determine the reconstruction. It turns out that the entire algorithm to discretize the induction equation to obtain the magnetic field approximation can be equivalently reformulated to a form without any reconstruction. The magnetic fields will still be approximated by the exactly divergence-free $H(\text{div})$ -conforming BDM finite element functions as in [26,27] (see Sect. 2.2 for comments on the use of general $H(\text{div})$ -conforming finite element spaces), and the new challenge comes from the need for numerical fluxes to approximate the electric field on element interfaces and at vertices.

It is known that the choices of numerical fluxes play an important role for the accuracy and stability of DG methods. To finalize our methods, we first identify two necessary conditions (see Theorem 3.1) on the numerical fluxes used in the different parts of the numerical methods, to ensure the reconstructed magnetic field is exactly divergence-free. We then adapt the proposed methods to a constant coefficient linear model, the induction equation with a given constant velocity field, and carry out both a numerical study and a Fourier analysis, to learn about the choices of numerical fluxes for the electric field especially at the mesh vertices, and their roles to the accuracy and numerical stability of the methods. Even though such study is only for a linear model for the magnetic field, the experience we have with it informs us how to choose numerical fluxes (see Sect. 4.3) for the proposed schemes to solve the full ideal MHD equations accurately and robustly. Our final choice of the electric field flux at mesh vertices is one type of multi-dimensional Riemann solver used in [7]. Our numerical tests in Sect. 4.1 imply that multi-dimensional Riemann solvers, when they introduce enough numerical dissipation, can make a good approximation to the electric field flux at vertices. Multi-dimensional Riemann solvers have been used within the WENO finite volume method frameworks in [4–6] to solve ideal MHD equations.

The rest of this paper is organized as follows. In Sect. 2, we describe the ideal MHD equations and introduce notations for meshes and discrete spaces. In Sect. 3, we present the proposed DG methods, and identify the conditions on the numerical fluxes to ensure the overall algorithms to be exactly divergence-free. In order to know what choices of numerical fluxes, especially for the electric field on element interfaces and at vertices, will render accurate and stable algorithms, in Sect. 4 we adapt the proposed methods to the induction equation and carry out numerical and analytical studies. In Sect. 5, nonlinear limiters are discussed, and the entire algorithm is also presented. Numerical examples are presented in Sect. 6 to illustrate the performance of the proposed methods, and this is followed by concluding remarks in Sect. 7.

2 MHD Equations, Notations and Discrete Spaces

2.1 MHD Equations

We consider the ideal MHD equations consisting of a set of nonlinear hyperbolic conservation laws

$$\frac{\partial \rho}{\partial t} + \nabla \cdot (\rho \mathbf{u}) = 0, \tag{1}$$

$$\frac{\partial (\rho \mathbf{u})}{\partial t} + \nabla \cdot \left[\rho \mathbf{u} \mathbf{u}^T + \left(p + \frac{1}{2} |\mathbf{B}|^2 \right) \mathbf{I} - \mathbf{B} \mathbf{B}^T \right] = 0, \tag{2}$$

$$\frac{\partial \mathbf{B}}{\partial t} - \nabla \times (\mathbf{u} \times \mathbf{B}) = 0, \tag{3}$$

$$\frac{\partial \mathcal{E}}{\partial t} + \nabla \cdot \left[\left(\mathcal{E} + p + \frac{1}{2} |\mathbf{B}|^2 \right) \mathbf{u} - \mathbf{B} (\mathbf{u} \cdot \mathbf{B}) \right] = 0, \tag{4}$$

with a divergence-free constraint

$$\nabla \cdot \mathbf{B} = 0. \tag{5}$$

Here ρ is the density, p is the hydrodynamic pressure, $\mathbf{u} = (u_x, u_y, u_z)^T$ is the velocity, and $\mathbf{B} = (B_x, B_y, B_z)^T$ is the magnetic field. The total energy is given by $\mathcal{E} = \frac{1}{2} \rho |\mathbf{u}|^2 + \frac{1}{2} |\mathbf{B}|^2 + \frac{p}{\gamma - 1}$ with γ as the ratio of the specific heats. The superscript T denotes the vector transpose. \mathbf{I} is the identity matrix, $\nabla \cdot$ is the divergence operator, and $\nabla \times$ is the curl operator. In two dimensions, all functions depend on the spatial variables x and y . Hence only B_x and B_y contribute to $\nabla \cdot \mathbf{B}$. The Eqs. (1)–(4) can be written as

$$\frac{\partial \mathbf{U}}{\partial t} + \nabla \cdot \mathbf{F}(\mathbf{U}, \mathcal{B}) = 0, \tag{6}$$

$$\frac{\partial \mathcal{B}}{\partial t} + \widehat{\nabla} \times E_z(\mathbf{U}, \mathcal{B}) = 0, \tag{7}$$

where $\mathbf{U} = (\rho, \rho u_x, \rho u_y, \rho u_z, B_x, B_y, \mathcal{E})^T$, $\mathcal{B} = (B_x, B_y)^T$, and $\mathbf{F} = (F_1, F_2)$ with

$$F_1(\mathbf{U}, \mathcal{B}) = \left(\rho u_x, \rho u_x^2 + p + \frac{1}{2} |\mathbf{B}|^2 - B_x^2, \rho u_x u_y - B_x B_y, \rho u_x u_z - B_x B_z, u_x B_z - u_z B_x, u_x \left(\mathcal{E} + p + \frac{1}{2} |\mathbf{B}|^2 \right) - B_x (\mathbf{u} \cdot \mathbf{B}) \right)^T, \tag{8}$$

$$F_2(\mathbf{U}, \mathcal{B}) = \left(\rho u_y, \rho u_x u_y - B_x B_y, \rho u_y^2 + p + \frac{1}{2} |\mathbf{B}|^2 - B_y^2, \rho u_y u_z - B_y B_z, u_y B_z - u_z B_y, u_y \left(\mathcal{E} + p + \frac{1}{2} |\mathbf{B}|^2 \right) - B_y (\mathbf{u} \cdot \mathbf{B}) \right)^T. \tag{9}$$

In addition, $E_z(\mathbf{u}, \mathcal{B}) = u_y B_x - u_x B_y$ which is the z-component of the electric field $\mathbf{E} = -\mathbf{u} \times \mathbf{B}$, and $\widehat{\nabla} \times E_z = \left(\frac{\partial E_z}{\partial y}, -\frac{\partial E_z}{\partial x} \right)^T$ is the first two components of $\nabla \times (0, 0, E_z)^T$. Without confusion, we will refer to \mathcal{B} as the magnetic field.

2.2 Notations and Discrete Spaces

In this subsection, notations and discrete spaces for numerical schemes are introduced. We assume the computational domain is $\Omega = [x_{min}, x_{max}] \times [y_{min}, y_{max}] \subset \mathbb{R}^d$ with $d = 2$. Let

$\{x_i\}_i$ and $\{y_j\}_j$ be the partitions of $[x_{min}, x_{max}]$ and $[y_{min}, y_{max}]$, respectively. We define $x_{i+\frac{1}{2}} = \frac{1}{2}(x_i + x_{i+1})$, $y_{j+\frac{1}{2}} = \frac{1}{2}(y_j + y_{j+1})$ and $I_{ij} = [x_{i-\frac{1}{2}}, x_{i+\frac{1}{2}}] \times [y_{j-\frac{1}{2}}, y_{j+\frac{1}{2}}]$ as an rectangle element with (x_i, y_j) as the center. Let $\Delta x = x_{i+\frac{1}{2}} - x_{i-\frac{1}{2}}$, $\Delta y = y_{j+\frac{1}{2}} - y_{j-\frac{1}{2}}$, and let $\mathcal{T}_h = \bigcup_{ij} I_{ij}$ be a partition of the domain Ω .

The discrete spaces are defined over the mesh. For variable \mathbf{U} , we use the piecewise polynomial vector space

$$\mathcal{V}_h^k = \left\{ \mathbf{v}: \mathbf{v}|_K \in [P^k(K)]^{8-d}, \forall K \in \mathcal{T}_h \right\}, \tag{10}$$

where $P^k(K)$ is the space of polynomials with the total degree at most k in K , and $[P^k(K)]^n$ is its vector version. For the magnetic field \mathcal{B} , we approximate it using globally (also called exactly) divergence-free polynomial functions, which are piecewise divergence-free with continuous normal components across element interfaces. This space is defined as

$$\begin{aligned} \mathcal{M}_h^k &= \left\{ \mathbf{v} \in H(\text{div}^0; \Omega): \mathbf{v}|_K \in \mathcal{W}^k(K), \forall K \in \mathcal{T}_h \right\} \\ &= \left\{ \mathbf{v}: \mathbf{v}|_K \in \mathcal{W}^k(K), \nabla \cdot \mathbf{v}|_K = 0, \forall K \in \mathcal{T}_h, \right. \end{aligned} \tag{11}$$

and the normal component of \mathbf{v} is continuous across each element interface $\left. \right\}$,

with $\mathcal{W}^k(K)$ defined as

$$\mathcal{W}^k(K) = [P^k(K)]^d \oplus \text{span} \left\{ \widehat{\nabla} \times (x^{k+1}y), \widehat{\nabla} \times (xy^{k+1}) \right\}. \tag{12}$$

\mathcal{M}_h^k is the divergence-free subspace of the $H(\text{div})$ -conforming Brezzi–Douglas–Marini (BDM) finite element space

$$\text{BDM}^k = \left\{ \mathbf{v} \in H(\text{div}): \mathbf{v}|_K \in \mathcal{W}^k(K), \forall K \in \mathcal{T}_h \right\}, \tag{13}$$

and it has optimal accuracy to approximate functions in $H(\text{div}^0) = \{\mathbf{v} \in [L^2(\Omega)]^d: \nabla \cdot \mathbf{v} = 0\}$ [10]. As pointed out in [26], divergence-free subspaces of other $H(\text{div})$ -conforming finite element spaces, such as Brezzi–Douglas–Fortin–Marini (BDFM) [11] or Raviart–Thomas (RT) [32] finite element spaces can also be used to provide divergence-free approximations for the magnetic field by following the same framework proposed in the present paper. The BDM finite element space is chosen here as it is the smallest among these candidates to achieve the same order of accuracy in the L^2 norm.

3 Proposed Numerical Methods for Ideal MHD Equations

In this section, we will formulate the DG methods with a globally divergence-free magnetic field to solve the MHD equations (6)–(7). For simplicity, we use the forward Euler method as time discretization to present the schemes. For high order accuracy in time, strong-stability-preserving Runge–Kutta methods will be used [21]. Such time integrators can be expressed as convex combinations of the forward Euler method, and hence they preserve the globally divergence-free property of the magnetic field. To describe the proposed methods, we assume the numerical solutions at time $t = t_n$ are available, that is $(\mathbf{U}_h^n, \mathcal{B}_h^n) \in \mathcal{V}_h^k \times \mathcal{M}_h^k$ with $\mathcal{B}_h^n = (B_{x,h}^n, B_{y,h}^n)^T$. We want to compute the numerical solutions at $t_{n+1} = t_n + \Delta t$, denoted as $(\mathbf{U}_h^{n+1}, \mathcal{B}_h^{n+1}) \in \mathcal{V}_h^k \times \mathcal{M}_h^k$ with $\mathcal{B}_h^{n+1} = (B_{x,h}^{n+1}, B_{y,h}^{n+1})^T$.

3.1 DG Methods to Update U_h^{n+1}

We update the variable U_h^{n+1} by applying to (6) the standard DG method [16] as the spatial discretization and forward Euler method as the time discretization. That is, we look for $U_h^{n+1} \in \mathcal{V}_h^k$, such that for any $w \in \mathcal{V}_h^k$ and any element $I_{ij} \in \mathcal{T}_h$,

$$\int_{I_{ij}} U_h^{n+1} \cdot w dx dy = \int_{I_{ij}} U_h^n \cdot w dx dy - \Delta t \left(\int_{\partial I_{ij}} \mathbf{H}_{e,I_{ij}}(\mathbf{v}^{int(I_{ij})}, \mathbf{v}^{ext(I_{ij})}; \mathbf{n}) \cdot w ds - \int_{I_{ij}} \mathbf{F}(U_h^n, \mathcal{B}_h^n) \cdot \nabla w dx dy \right). \tag{14}$$

Here, $\mathbf{H}_{e,I_{ij}}(\mathbf{v}^{int(I_{ij})}, \mathbf{v}^{ext(I_{ij})}; \mathbf{n})$ is the numerical flux to approximate $\mathbf{F}(U, \mathcal{B}) \cdot \mathbf{n}$, and $\mathbf{n} = (n_1, n_2)^T$ is the outward normal vector of an edge e of the element I_{ij} . \mathbf{v} is a symbol which denotes the variables (U_h^n, \mathcal{B}_h^n) , and $\mathbf{v}^{int(I_{ij})}, \mathbf{v}^{ext(I_{ij})}$ are the limits of \mathbf{v} from the interior and exterior of an element I_{ij} along its edge e . In our simulation, we take the Lax–Friedrichs numerical flux

$$\mathbf{H}_{e,I_{ij}}(\mathbf{a}, \mathbf{b}; \mathbf{n}) = \frac{1}{2} (\mathbf{F}(\mathbf{a}) \cdot \mathbf{n} + \mathbf{F}(\mathbf{b}) \cdot \mathbf{n} - \alpha(\mathbf{b} - \mathbf{a})), \tag{15}$$

where α is an estimate of the maximal absolute eigenvalue of the Jacobian $\frac{\partial \mathbf{F}(U, \mathcal{B}) \cdot \mathbf{n}}{\partial (U, \mathcal{B})}$ in the neighborhood of the edge e .

3.2 DG Methods for Globally Divergence-Free Magnetic Field \mathcal{B}

In this subsection, we present DG methods for the induction equation (7) to generate a globally divergence-free approximation $\mathcal{B}_h^{n+1} = (B_{x,h}^{n+1}, B_{y,h}^{n+1})^T \in \mathcal{M}_h^k$ for the magnetic field \mathcal{B} . It is known that a piecewise divergence-free vector field is globally divergence-free if its normal component is continuous on element interfaces. Therefore, we first approximate the normal component of the magnetic field $\mathcal{B} \cdot \mathbf{n}$ on element interfaces based on the DG methods (see Sect. 3.2.1). Then, an element by element reconstruction is used to reconstruct the globally divergence-free magnetic field (see Sect. 3.2.3). When $k \geq 2$, more information about the magnetic field is obtained by approximating the two-dimensional system (7) using a standard DG method that is *less* accurate (see Sect. 3.2.2). In Sect. 3.2.4, we will present a reformulation of the schemes, equivalent to that in Sects. 3.2.1–3.2.3 to update the magnetic field yet free of reconstruction. Throughout this subsection, E_z in numerical schemes and its related numerical fluxes are from time t_n .

3.2.1 Approximation of $\mathcal{B} \cdot \mathbf{n}$ on the Element Interfaces

To get the continuous normal component $\mathcal{B} \cdot \mathbf{n}$ of the magnetic field, we formulate a DG-type scheme for magnetic field equations on the element interfaces. For the rectangular mesh, $\mathcal{B} \cdot \mathbf{n}$ is $B_{x,h}^{n+1}$ along y -direction edges with $\mathbf{n} = (1, 0)^T$, and it is $B_{y,h}^{n+1}$ along the x -direction edges with $\mathbf{n} = (0, 1)^T$.

To propose the DG method for Eq. (7) on the element interface, we consider the equation

$$\frac{\partial \mathcal{B} \cdot \mathbf{n}}{\partial t} + \widehat{\nabla} \times E_z(U, \mathcal{B}) \cdot \mathbf{n} = 0. \tag{16}$$

To this end, on a rectangular mesh, we need to consider two one-dimensional equations of the system (16)

$$\frac{\partial B_x}{\partial t} + \frac{\partial E_z}{\partial y} = 0, \tag{17}$$

$$\frac{\partial B_y}{\partial t} - \frac{\partial E_z}{\partial x} = 0. \tag{18}$$

We use the DG method as the spatial discretization and forward Euler method as the time discretization for Eqs. (17) and (18) on element interfaces. The method is as follows: look for $b_{ij}^x(y) \in P^k([y_{j-\frac{1}{2}}, y_{j+\frac{1}{2}}])$, such that for any $\varphi(y) \in P^k([y_{j-\frac{1}{2}}, y_{j+\frac{1}{2}}])$

$$\int_{y_{j-\frac{1}{2}}}^{y_{j+\frac{1}{2}}} b_{ij}^x(y)\varphi(y)dy = \int_{y_{j-\frac{1}{2}}}^{y_{j+\frac{1}{2}}} B_x^n(x_{i+\frac{1}{2}}, y)\varphi(y)dy - \Delta t \left(\widehat{E}_z(x_{i+\frac{1}{2}}, y)\varphi(y) \Big|_{y_{j-\frac{1}{2}}}^{y_{j+\frac{1}{2}}} - \int_{y_{j-\frac{1}{2}}}^{y_{j+\frac{1}{2}}} \overline{E}_z(x_{i+\frac{1}{2}}, y) \frac{\partial \varphi(y)}{\partial y} dy \right), \tag{19}$$

and look for $b_{ij}^y(x) \in P^k([x_{i-\frac{1}{2}}, x_{i+\frac{1}{2}}])$, such that for any $\varphi(x) \in P^k([x_{i-\frac{1}{2}}, x_{i+\frac{1}{2}}])$

$$\int_{x_{i-\frac{1}{2}}}^{x_{i+\frac{1}{2}}} b_{ij}^y(x)\varphi(x)dx = \int_{x_{i-\frac{1}{2}}}^{x_{i+\frac{1}{2}}} B_y^n(x, y_{j+\frac{1}{2}})\varphi(x)dx - \Delta t \left(\widehat{\overline{E}}_z(x, y_{j+\frac{1}{2}})\varphi(x) \Big|_{x_{i-\frac{1}{2}}}^{x_{i+\frac{1}{2}}} - \int_{x_{i-\frac{1}{2}}}^{x_{i+\frac{1}{2}}} \overline{\overline{E}}_z(x, y_{j+\frac{1}{2}}) \frac{\partial \varphi(x)}{\partial x} dx \right). \tag{20}$$

Here b_{ij}^x and b_{ij}^y denote the approximations of $B_x(x_{i+\frac{1}{2}}, y)$ for $y \in [y_{j-\frac{1}{2}}, y_{j+\frac{1}{2}}]$ and $B_y(x, y_{j+\frac{1}{2}})$ for $x \in [x_{i-\frac{1}{2}}, x_{i+\frac{1}{2}}]$ at time $t = t_{n+1}$, respectively. \widehat{E}_z and $\widehat{\overline{E}}_z$ are exact or approximate Riemann solvers to approximate the electric field flux E_z at the vertices of a mesh element, while \overline{E}_z , $\overline{\overline{E}}_z$ are exact or approximate Riemann solvers to approximate E_z on the element interfaces, and their choices will be discussed in Theorem 3.1 and specified in Sect. 4.3. $\{b_{ij}^x\}_{ij}$ and $\{b_{ij}^y\}_{ij}$ will be used to reconstruct the globally divergence-free magnetic field.

3.2.2 Additional Information for the Magnetic Field \mathcal{B} : $\widetilde{\mathcal{B}}_h$ in Mesh Elements

When $k \geq 2$, $\{b_{ij}^x\}_{ij}$ and $\{b_{ij}^y\}_{ij}$ do not provide enough information to reconstruct a two-dimensional function in \mathcal{N}_h^k . For more information, a standard DG method with lower accuracy is applied to the two-dimensional system (7). For $k \geq 2$, we look for

$\widetilde{\mathcal{B}}_h \in [P^{k-2}(I_{ij})]^2$ such that for any $\Phi \in [P^{k-2}(I_{ij})]^2$ with $\Phi = (\Phi_1, \Phi_2)^T$,

$$\begin{aligned} \int_{I_{ij}} \widetilde{\mathcal{B}}_h \cdot \Phi dx dy &= \int_{I_{ij}} \mathcal{B}_h^n \cdot \Phi dx dy \\ &- \Delta t \left(\int_{x_{i-\frac{1}{2}}}^{x_{i+\frac{1}{2}}} (\widetilde{E}_z \Phi_1)(x, y_{j+\frac{1}{2}}) dx - \int_{x_{i-\frac{1}{2}}}^{x_{i+\frac{1}{2}}} (\widetilde{E}_z \Phi_1)(x, y_{j-\frac{1}{2}}) dx \right. \\ &+ \int_{y_{j-\frac{1}{2}}}^{y_{j+\frac{1}{2}}} (\widetilde{-E}_z \Phi_2)(x_{i+\frac{1}{2}}, y) dy - \int_{y_{j-\frac{1}{2}}}^{y_{j+\frac{1}{2}}} (\widetilde{-E}_z \Phi_2)(x_{i-\frac{1}{2}}, y) dy \\ &\left. - \int_{I_{ij}} \left(E_z \frac{\partial \Phi_1}{\partial y} - E_z \frac{\partial \Phi_2}{\partial x} \right) dx dy \right). \end{aligned} \tag{21}$$

Here \widetilde{E}_z is the numerical flux for $E_z = (0, E_z)^T \cdot \mathbf{n}$ with $\mathbf{n} = (0, 1)^T$ along an x -direction edge, and $\widetilde{-E}_z$ is the numerical flux for $-E_z = (-E_z, 0)^T \cdot \mathbf{n}$ with $\mathbf{n} = (1, 0)^T$ along a y -direction edge. Both \widetilde{E}_z and $\widetilde{-E}_z$ will be taken as the one-dimensional Lax–Friedrichs flux (15). It will be seen from Theorem 3.1 that the numerical fluxes \widetilde{E}_z and $\widetilde{-E}_z$ in (19)–(20) need to be related to \widetilde{E}_z and $\widetilde{-E}_z$ in order to ensure the globally divergence-free reconstruction, also see Sect. 4.3.

3.2.3 Reconstruct the Globally Divergence-Free Magnetic Field \mathcal{B}_h^{n+1}

Once we have $\{b_{ij}^x\}_{ij}, \{b_{ij}^y\}_{ij}$ on element interfaces from (19) and (20) as well as $\widetilde{\mathcal{B}}_h$ from (21), we will follow the idea of the BDM projection [10] (also see [26, 27]) to carry out an element-by-element reconstruction of a globally divergence-free magnetic field \mathcal{B}_h^{n+1} . Given an element I_{ij} , the reconstruction is to obtain $\mathcal{B}_h^{n+1}|_{I_{ij}} \in \mathcal{W}^k(I_{ij})$ on I_{ij} , such that $\mathcal{B}_h^{n+1} = (B_{x,h}^{n+1}, B_{y,h}^{n+1})^T$ satisfies

- R1** $\int_{y_{j-\frac{1}{2}}}^{y_{j+\frac{1}{2}}} (B_{x,h}^{n+1}(x_{l+\frac{1}{2}}, y) - b_{lj}^x(y)) \varphi(y) dy = 0$ on the y -direction edge with $l = i - 1, i$ and any $\varphi(y) \in P^k([y_{j-\frac{1}{2}}, y_{j+\frac{1}{2}}])$,
- R2** $\int_{x_{i-\frac{1}{2}}}^{x_{i+\frac{1}{2}}} (B_{y,h}^{n+1}(x, y_{l+\frac{1}{2}}) - b_{il}^y(x)) \varphi(x) dx = 0$ on the x -direction edge with $l = j - 1, j$ and any $\varphi(x) \in P^k([x_{i-\frac{1}{2}}, x_{i+\frac{1}{2}}])$,
- R3** $\int_{I_{ij}} (\mathcal{B}_h^{n+1}(x, y) - \widetilde{\mathcal{B}}_h(x, y)) \Phi(x, y) dx dy = 0$ for any $\Phi(x, y) \in [P^{k-2}(I_{ij})]^2$ when $k \geq 2$.

From the reconstruction, one can see that the normal component of the magnetic field \mathcal{B}_h^{n+1} , given by $\{b_{ij}^x\}_{ij}$ or $\{b_{ij}^y\}_{ij}$, is single-valued, and hence it is continuous on element interfaces. When $k \geq 2$, additional information is provided by $\widetilde{\mathcal{B}}_h$ via L^2 projection. In the next theorem, we will show that the reconstruction produces a globally divergence-free approximation for the magnetic field under some conditions for the numerical fluxes in schemes (19)–(21).

Theorem 3.1 *Under the conditions that*

1. the electric field flux approximations in (19)–(21) along the same edge satisfy

$$\overline{E_z} = -(\widetilde{-E_z}), \quad \overline{\overline{-E_z}} = -(\widetilde{E_z}), \tag{22}$$

2. and the electric field flux approximations in (19)–(20) at the same vertex is single-valued, satisfying

$$\widehat{\overline{-E_z}} = -\widehat{E_z}, \tag{23}$$

then for any $k \geq 0$, the reconstructed $\mathfrak{B}_h^{n+1}(I_{ij})$ exists uniquely in $\mathcal{W}^k(I_{ij})$. In addition, $\nabla \cdot \mathfrak{B}_h^{n+1}|_{I_{ij}} = 0$.

Proof One can follow the same proof as in [26] to show the unique existence of the reconstructed $\mathfrak{B}_h^{n+1}(I_{ij}) \in \mathcal{W}^k(I_{ij})$. We here will only show the divergence-free property of \mathfrak{B}_h^{n+1} .

For any $\omega \in P^{k-1}(I_{ij})$, from the reconstruction step **R3** and equation (21), we have

$$\begin{aligned} \int_{I_{ij}} \mathfrak{B}_h^{n+1} \nabla \omega dx dy &= \int_{I_{ij}} \widetilde{\mathfrak{B}}_h \nabla \omega dx dy \\ &= \int_{I_{ij}} \mathfrak{B}_h^n \nabla \omega dx dy - \Delta t \left(\Theta_{inside} - \int_{I_{ij}} \left(E_z \frac{\partial^2 \omega}{\partial x \partial y} - E_z \frac{\partial^2 \omega}{\partial y \partial x} \right) dx dy \right) \\ &= \int_{I_{ij}} \mathfrak{B}_h^n \nabla \omega dx dy - \Delta t \Theta_{inside}, \end{aligned} \tag{24}$$

where

$$\begin{aligned} \Theta_{inside} &= \int_{x_{i-\frac{1}{2}}}^{x_{i+\frac{1}{2}}} \left(\widetilde{E_z} \frac{\partial \omega}{\partial x} \right) (x, y_{j+\frac{1}{2}}) dx - \int_{x_{i-\frac{1}{2}}}^{x_{i+\frac{1}{2}}} \left(\widetilde{E_z} \frac{\partial \omega}{\partial x} \right) (x, y_{j-\frac{1}{2}}) dx \\ &\quad + \int_{y_{j-\frac{1}{2}}}^{y_{j+\frac{1}{2}}} \left(\widetilde{\overline{-E_z}} \frac{\partial \omega}{\partial y} \right) (x_{i+\frac{1}{2}}, y) dy - \int_{y_{j-\frac{1}{2}}}^{y_{j+\frac{1}{2}}} \left(\widetilde{\overline{-E_z}} \frac{\partial \omega}{\partial y} \right) (x_{i-\frac{1}{2}}, y) dy, \end{aligned}$$

and $\mathfrak{B}_h^n \in \mathcal{M}_h^k$ is the globally divergence-free approximation of \mathfrak{B} at time t_n .

From the reconstruction steps **R1** and **R2**, we have

$$\begin{aligned} \int_{\partial I_{ij}} \mathfrak{B}_h^{n+1} \cdot \mathbf{n} \omega ds &= \int_{x_{i-\frac{1}{2}}}^{x_{i+\frac{1}{2}}} b_{ij}^y(x) \omega(x, y_{j+\frac{1}{2}}) dx - \int_{x_{i-\frac{1}{2}}}^{x_{i+\frac{1}{2}}} b_{ij-1}^y(x) \omega(x, y_{j-\frac{1}{2}}) dx \\ &\quad + \int_{y_{j-\frac{1}{2}}}^{y_{j+\frac{1}{2}}} b_{ij}^x(y) \omega(x_{i+\frac{1}{2}}, y) dy - \int_{y_{j-\frac{1}{2}}}^{y_{j+\frac{1}{2}}} b_{i-1j}^x(y) \omega(x_{i-\frac{1}{2}}, y) dy. \end{aligned} \tag{25}$$

With the schemes (19) and (20), we further get

$$\int_{\partial I_{ij}} \mathfrak{B}_h^{n+1} \cdot \mathbf{n} \omega ds = \int_{\partial I_{ij}} \mathfrak{B}_h^n \cdot \mathbf{n} \omega ds + \Delta t (\Theta_{edge} - \Theta_{vertex}), \tag{26}$$

with

$$\begin{aligned} \Theta_{edge} &= \int_{y_{j-\frac{1}{2}}}^{y_{j+\frac{1}{2}}} \left(\overline{E_z} \frac{\partial \omega}{\partial y} \right) (x_{i+\frac{1}{2}}, y) dy - \int_{y_{j-\frac{1}{2}}}^{y_{j+\frac{1}{2}}} \left(\overline{E_z} \frac{\partial \omega}{\partial y} \right) (x_{i-\frac{1}{2}}, y) dy \\ &\quad + \int_{x_{i-\frac{1}{2}}}^{x_{i+\frac{1}{2}}} \left(\overline{\overline{-E_z}} \frac{\partial \omega}{\partial x} \right) (x, y_{j+\frac{1}{2}}) dx - \int_{x_{i-\frac{1}{2}}}^{x_{i+\frac{1}{2}}} \left(\overline{\overline{-E_z}} \frac{\partial \omega}{\partial x} \right) (x, y_{j-\frac{1}{2}}) dx, \end{aligned}$$

and

$$\begin{aligned} \Theta_{vertex} &= \left(\widehat{E_z\omega}\right)(x_{i+\frac{1}{2}}, y_{j+\frac{1}{2}}) - \left(\widehat{E_z\omega}\right)(x_{i+\frac{1}{2}}, y_{j-\frac{1}{2}}) \\ &\quad - \left(\widehat{E_z\omega}\right)(x_{i-\frac{1}{2}}, y_{j+\frac{1}{2}}) + \left(\widehat{E_z\omega}\right)(x_{i-\frac{1}{2}}, y_{j-\frac{1}{2}}) \\ &\quad + \left(\widehat{-E_z\omega}\right)(x_{i+\frac{1}{2}}, y_{j+\frac{1}{2}}) - \left(\widehat{-E_z\omega}\right)(x_{i-\frac{1}{2}}, y_{j+\frac{1}{2}}) \\ &\quad - \left(\widehat{-E_z\omega}\right)(x_{i+\frac{1}{2}}, y_{j-\frac{1}{2}}) + \left(\widehat{-E_z\omega}\right)(x_{i-\frac{1}{2}}, y_{j-\frac{1}{2}}). \end{aligned}$$

Under the condition in (23) that the electric field flux approximations at vertices are single-valued, we have $\Theta_{vertex} = 0$. Moreover, under the condition (22), we get $\Theta_{edge} + \Theta_{inside} = 0$. Now we can apply Gauss theorem, utilize the relations in (24) and (26), and get

$$\begin{aligned} \int_{I_{ij}} \nabla \cdot \mathcal{B}_h^{n+1} \omega dx dy &= \int_{\partial I_{ij}} \mathcal{B}_h^{n+1} \cdot \mathbf{n} \omega ds - \int_{I_{ij}} \mathcal{B}_h^{n+1} \nabla \omega dx dy \\ &= \int_{\partial I_{ij}} \mathcal{B}_h^n \cdot \mathbf{n} \omega ds - \int_{I_{ij}} \mathcal{B}_h^n \nabla \omega dx dy + \Delta t (\Theta_{edge} + \Theta_{inside} - \Theta_{vertex}) \\ &= \int_{I_{ij}} \nabla \cdot \mathcal{B}_h^n \omega dx dy + \Delta t (\Theta_{edge} + \Theta_{inside} - \Theta_{vertex}) = 0. \end{aligned} \tag{27}$$

Here we have used the fact that $\nabla \cdot \mathcal{B}_h^n = 0$ at time t_n . Finally, note that $\nabla \cdot \mathcal{B}_h^{n+1} \in P^{k-1}(I_{ij})$, by taking $\omega = \nabla \cdot \mathcal{B}_h^{n+1}$ in (27), we conclude $\nabla \cdot \mathcal{B}_h^{n+1} = 0$. □

Remark 3.2 Two conditions (22)–(23) are needed to ensure the exactly divergence-free reconstructions. The one in (23) that requires a single-valued electric field flux approximation at vertices has long been used for many constrained transport methods in various frameworks such as finite difference and finite volume methods, while the condition in (22) is needed only in finite element type of methods including DG methods. Both conditions can be avoided if central DG methods are used, see [26,27].

3.2.4 Equivalent form of Numerical Schemes for \mathcal{B}_h^{n+1} : Without Reconstruction

From the reconstruction **R1–R3** in Sect. 3.2.3, one can see that the normal components of \mathcal{B}_h^{n+1} along the edges of an element are identical to b_{ij}^x and b_{ij}^y (at most up to a sign difference, or a shift in index i or j), and its L^2 projection onto $[P^{k-2}(I_{ij})]^2$ is identical to $\widetilde{\mathcal{B}}_h$. Therefore the schemes to compute the globally divergence-free $\mathcal{B}_h^{n+1} = (B_{x,h}^{n+1}, B_{y,h}^{n+1})^T \in \mathcal{M}_h^k$ in Sects. 3.2.1–3.2.3 can be rewritten into an equivalent formulation as follows, *without* any reconstruction: look for $\mathcal{B}_h^{n+1} = (B_{x,h}^{n+1}, B_{y,h}^{n+1})^T$ such that $\mathcal{B}_h^{n+1}|_{I_{ij}} \in \mathcal{W}^k(I_{ij})$ for any i, j , satisfying

$$\begin{aligned} \int_{y_{j-\frac{1}{2}}}^{y_{j+\frac{1}{2}}} B_{x,h}^{n+1}(x_{l+\frac{1}{2}}, y) \varphi(y) dy &= \int_{y_{j-\frac{1}{2}}}^{y_{j+\frac{1}{2}}} B_x^n(x_{l+\frac{1}{2}}, y) \varphi(y) dy \\ &\quad - \Delta t \left(\widehat{E_z}(x_{l+\frac{1}{2}}, y) \varphi(y) \Big|_{y_{j-\frac{1}{2}}}^{y_{j+\frac{1}{2}}} - \int_{y_{j-\frac{1}{2}}}^{y_{j+\frac{1}{2}}} \overline{E_z}(x_{l+\frac{1}{2}}, y) \frac{\partial \varphi(y)}{\partial y} dy \right) \end{aligned} \tag{28}$$

for any $\varphi(y) \in P^k([y_{j-\frac{1}{2}}, y_{j+\frac{1}{2}}])$ and with $l = i - 1, i$;

$$\int_{x_{i-\frac{1}{2}}}^{x_{i+\frac{1}{2}}} \mathcal{B}_{y,h}^{n+1}(x, y_{l+\frac{1}{2}}) \varphi(x) dx = \int_{x_{i-\frac{1}{2}}}^{x_{i+\frac{1}{2}}} \mathcal{B}_y^n(x, y_{l+\frac{1}{2}}) \varphi(x) dx - \Delta t \left(\widetilde{\overline{\overline{E_z}}}(x, y_{l+\frac{1}{2}}) \varphi(x) \Big|_{x_{i-\frac{1}{2}}}^{x_{i+\frac{1}{2}}} - \int_{x_{i-\frac{1}{2}}}^{x_{i+\frac{1}{2}}} \overline{\overline{E_z}}(x, y_{l+\frac{1}{2}}) \frac{\partial \varphi(x)}{\partial x} dx \right) \tag{29}$$

for any $\varphi(x) \in P^k([x_{i-\frac{1}{2}}, x_{i+\frac{1}{2}}])$ and with $l = j - 1, j$; in addition,

$$\int_{I_{ij}} \mathcal{B}_h^{n+1} \cdot \Phi dx dy = \int_{I_{ij}} \mathcal{B}_h^n \Phi dx dy - \Delta t \left(\int_{x_{i-\frac{1}{2}}}^{x_{i+\frac{1}{2}}} (\widetilde{\overline{\overline{E_z}}}\Phi_1)(x, y_{j+\frac{1}{2}}) dx - \int_{x_{i-\frac{1}{2}}}^{x_{i+\frac{1}{2}}} (\widetilde{\overline{\overline{E_z}}}\Phi_1)(x, y_{j-\frac{1}{2}}) dx + \int_{y_{j-\frac{1}{2}}}^{y_{j+\frac{1}{2}}} (\widetilde{\overline{\overline{E_z}}}\Phi_2)(x_{i+\frac{1}{2}}, y) dy - \int_{y_{j-\frac{1}{2}}}^{y_{j+\frac{1}{2}}} (\widetilde{\overline{\overline{E_z}}}\Phi_2)(x_{i-\frac{1}{2}}, y) dy - \int_{I_{ij}} \left(E_z \frac{\partial \Phi_1}{\partial y} - E_z \frac{\partial \Phi_2}{\partial x} \right) dx dy \right) \tag{30}$$

for any $\Phi \in [P^{k-2}(I_{ij})]^2$ with $\Phi = (\Phi_1, \Phi_2)^T$. Again the numerical fluxes will satisfy the two conditions (22)–(23). Theorem 3.1 ensures that the resulting magnetic field \mathcal{B}_h^{n+1} is in \mathcal{M}_h^k and hence globally divergence-free. (One should refer to equations (5.4) and (5.6) in [10] for a more direct analysis.)

Even though the reformulation of the schemes in this subsection is more straightforward, in the presence of strong discontinuities in the solutions, nonlinear limiters need to be applied to all unknowns, including the magnetic field (see Sect. 5 and the numerical example of cloud–shock interaction in Sect. 6.2.5). When nonlinear limiters are needed for the magnetic field, it is more flexible to work with the schemes in the formulation as in Sect. 3.2.1–3.2.3, so the limiters are applied *before* the reconstruction or a revised reconstruction, in order to still have a globally divergence-free approximation for the magnetic field.

4 How to Choose Electric Field Flux Approximations?

Theorem 3.1 suggests that electric field flux approximations used in the different parts of the proposed schemes (19)–(21) need to be single-valued at vertices and share the same formulas on the element interfaces. Just as in standard DG methods, choices of numerical fluxes are crucial for accuracy and robustness of the schemes. In this section, we want to investigate numerically and analytically on the choices of the electric field flux approximations. To this end, we will focus on the following equation for the magnetic field

$$\frac{\partial \mathcal{B}}{\partial t} + \widehat{\nabla} \times E_z(\mathbf{U}, \mathcal{B}) = 0. \tag{31}$$

Here $E_z = u_y B_x - u_x B_y$, with a constant velocity field (u_x, u_y) that is given. This system will be referred to as the induction equation. We will adapt the proposed schemes in Sect. 3.2 to the induction equation, and investigate numerically and analytically in next two subsections how different choices of electric field flux approximations affect accuracy and numerical

stability. Based on such study, in Sect. 4.3 we will specify our choices of the numerical fluxes in the proposed schemes (19)–(21) to compute the magnetic field.

4.1 Numerical Study

Adapting from the proposed schemes (19)–(21) and following the two required conditions (22)–(23) in Theorem 3.1, we consider the following schemes for the induction equation on the element interfaces, that is: look for $b_{ij}^x(y) \in P^k([y_{j-\frac{1}{2}}, y_{j+\frac{1}{2}}])$, such that for any $\varphi(y) \in P^k([y_{j-\frac{1}{2}}, y_{j+\frac{1}{2}}])$

$$\int_{y_{j-\frac{1}{2}}}^{y_{j+\frac{1}{2}}} b_{ij}^x(y)\varphi(y)dy = \int_{y_{j-\frac{1}{2}}}^{y_{j+\frac{1}{2}}} B_x^n(x_{i+\frac{1}{2}}, y)\varphi(y)dy - \Delta t \left(\widehat{E}_z(x_{i+\frac{1}{2}}, y)\varphi(y) \Big|_{y_{j-\frac{1}{2}}}^{y_{j+\frac{1}{2}}} + \int_{y_{j-\frac{1}{2}}}^{y_{j+\frac{1}{2}}} \widetilde{\widetilde{E}}_z(x_{i+\frac{1}{2}}, y) \frac{\partial \varphi(y)}{\partial y} dy \right), \tag{32}$$

and look for $b_{ij}^y(x) \in P^k([x_{i-\frac{1}{2}}, x_{i+\frac{1}{2}}])$, such that for any $\varphi(x) \in P^k([x_{i-\frac{1}{2}}, x_{i+\frac{1}{2}}])$

$$\int_{x_{i-\frac{1}{2}}}^{x_{i+\frac{1}{2}}} b_{ij}^y(x)\varphi(x)dx = \int_{x_{i-\frac{1}{2}}}^{x_{i+\frac{1}{2}}} B_y^n(x, y_{j+\frac{1}{2}})\varphi(x)dx - \Delta t \left(-\widehat{E}_z(x, y_{j+\frac{1}{2}})\varphi(x) \Big|_{x_{i-\frac{1}{2}}}^{x_{i+\frac{1}{2}}} + \int_{x_{i-\frac{1}{2}}}^{x_{i+\frac{1}{2}}} \widetilde{E}_z(x, y_{j+\frac{1}{2}}) \frac{\partial \varphi(x)}{\partial x} dx \right). \tag{33}$$

Corresponding to (21), the induction equation is further discretized as a two-dimensional system when $k \geq 2$: look for $\widetilde{\mathcal{B}}_h \in [P^{k-2}(I_{ij})]^2$ such that for any $\Phi = (\Phi_1, \Phi_2)^2 \in [P^{k-2}(I_{ij})]^2$,

$$\int_{I_{ij}} \widetilde{\mathcal{B}}_h \cdot \Phi dx dy = \int_{I_{ij}} \mathcal{B}_h^n \cdot \Phi dx dy - \Delta t \left(\int_{x_{i-\frac{1}{2}}}^{x_{i+\frac{1}{2}}} (\widetilde{E}_z \Phi_1)(x, y_{j+\frac{1}{2}}) dx - \int_{x_{i-\frac{1}{2}}}^{x_{i+\frac{1}{2}}} (\widetilde{E}_z \Phi_1)(x, y_{j-\frac{1}{2}}) dx + \int_{y_{j-\frac{1}{2}}}^{y_{j+\frac{1}{2}}} (\widetilde{\widetilde{E}}_z \Phi_2)(x_{i+\frac{1}{2}}, y) dy - \int_{y_{j-\frac{1}{2}}}^{y_{j+\frac{1}{2}}} (\widetilde{\widetilde{E}}_z \Phi_2)(x_{i-\frac{1}{2}}, y) dy - \int_{I_{ij}} \left(E_z \frac{\partial \Phi_1}{\partial y} - E_z \frac{\partial \Phi_2}{\partial x} \right) dx dy \right). \tag{34}$$

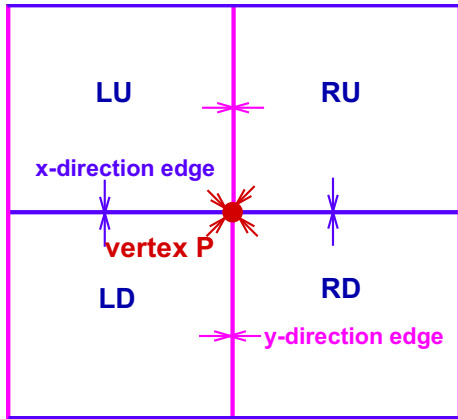
To help with the presentation, we illustrate the notations of states around a vertex \mathbf{P} , its neighboring elements, and the connected edges in Fig. 1. In (34), also in (32)–(33), \widetilde{E}_z and $\widetilde{\widetilde{E}}_z$ are taken as a one-dimensional Lax–Friedrichs flux. Namely, along an x -direction edge,

$$\widetilde{E}_z = \frac{E_z^{LD} + E_z^{LU}}{2} - \frac{\alpha_y}{2} (B_x^{LU} - B_x^{LD}), \tag{35}$$

and along a y -direction edge,

$$\widetilde{\widetilde{E}}_z = \frac{(-E_z^{RD} - E_z^{LD})}{2} - \frac{\alpha_x}{2} (B_y^{RD} - B_y^{LD}). \tag{36}$$

Fig. 1 The notations of states around a vertex **P**, its neighboring elements, and the connected edges



Here

$$\alpha_x = |u_x|, \quad \alpha_y = |u_y|, \tag{37}$$

and they are the largest absolute-value of eigenvalues of the Jacobian $\frac{\partial(0, -E_z)^T}{\partial(B_x, B_y)^T}$ and $\frac{\partial(E_z, 0)^T}{\partial(B_x, B_y)^T}$, respectively.

Just as in [3, 7, 8, 20], we use flux interpolations or approximate Riemann solvers to obtain the single-valued electric field flux \widehat{E}_z at vertex **P** used in (32)–(33). Particularly, we take

$$\begin{aligned} \widehat{E}_z &= \frac{1}{4} \left(\frac{E_z^{LD} + E_z^{LU}}{2} - \frac{\beta}{2} (B_x^{LU} - B_x^{LD}) \right) \\ &+ \frac{1}{4} \left(\frac{E_z^{RD} + E_z^{RU}}{2} - \frac{\beta}{2} (B_x^{RU} - B_x^{RD}) \right) \\ &+ \frac{1}{4} \left(\frac{E_z^{LD} + E_z^{RD}}{2} + \frac{\alpha}{2} (B_y^{RD} - B_y^{LD}) \right) \\ &+ \frac{1}{4} \left(\frac{E_z^{LU} + E_z^{RU}}{2} + \frac{\alpha}{2} (B_y^{RU} - B_y^{LU}) \right) \\ &= \frac{1}{4} (E_z^{LU} + E_z^{RU} + E_z^{LD} + E_z^{RD}) \\ &- \frac{\beta}{4} \left(\frac{B_x^{LU} + B_x^{RU}}{2} - \frac{B_x^{LD} + B_x^{RD}}{2} \right) \\ &+ \frac{\alpha}{4} \left(\frac{B_y^{RD} + B_y^{RU}}{2} - \frac{B_y^{LD} + B_y^{LU}}{2} \right). \end{aligned} \tag{38}$$

Here $\alpha = \sigma\alpha_x$ and $\beta = \sigma\alpha_y$, with the constant σ measures the amount of dissipation introduced by the numerical flux \widehat{E}_z , and α_x, α_y from (37). When $\alpha = \alpha_x, \beta = \alpha_y$, \widehat{E}_z is the arithmetic average of the one-dimensional Lax–Friedrichs flux, namely, an average with equal weight, 1/4, of the numerical fluxes in (35)–(36) from four edges connected to the vertex **P**. When $\alpha = 1.2\alpha_x$ and $\beta = 1.2\alpha_y$, \widehat{E}_z turns out to be the multi-dimensional HLL Riemann solver restricted at the vertex **P**, while \widehat{E}_z with $\alpha = 2\alpha_x$ and $\beta = 2\alpha_y$ is the

multi-dimensional Lax–Friedrichs Riemann solver restricted at \mathbf{P} . Both multi-dimensional Riemann solvers were used in [7].

Next we want to investigate numerically how the different choices of \widehat{E}_z will affect the performance of the numerical schemes (32)–(34) for the induction equation. We consider the same example as in [39], with the initial condition

$$(B_x, B_y) = (-\sin(2\pi y), \sin(2\pi x)),$$

and the constant velocity field is $(u_x, u_y) = (1, 1)$. Periodic boundary conditions are used. This example is computed on the domain $[0, 1] \times [0, 1]$ based on P^k approximations with $k = 0, 1, 2$. The third order TVD Runge–Kutta time discretization in (66) [21] is applied in time. The time step is determined as $\Delta t \leq CFL / \left(\frac{|u_x|}{\Delta x} + \frac{|u_y|}{\Delta y} \right)$ where the Courant–Friedrichs–Lewy (CFL) number CFL is taken to be 0.5, 0.2, 0.1 for $k = 0, 1, 2$, respectively. Table 1 shows the L^2 errors and orders of accuracy for the magnetic field component B_x at $t = 1.0$ and $t = 10$, computed by the methods (32)–(34) with different choices of the numerical fluxes. More specifically, \widehat{E}_z in (32)–(33) is evaluated as (38) with $\alpha = \sigma\alpha_x$ and $\beta = \sigma\alpha_y$, where $\alpha_x = \alpha_y = 1$, and $\sigma = 1, 1.2$, and 2. And \widetilde{E}_z and $\widetilde{\widetilde{E}}_z$ in (32)–(34) are from the one-dimensional Lax–Friedrichs flux (35)–(37). It is observed from Table 1 that when $\alpha = \alpha_x, \beta = \alpha_y$, the scheme is stable and first order accurate with P^0 approximation; With P^1 approximation, the scheme is only first order accurate which is suboptimal; while the scheme with P^2 approximation starts to be optimally accurate with third order accuracy and then shows instability over long time simulation. When $\alpha = 1.2\alpha_x$ and $\beta = 1.2\alpha_y$, the schemes have optimal accuracy with P^0 and P^1 approximations, yet with P^2 approximation the scheme becomes unstable at $t = 10$. When $\alpha = 2\alpha_x$ and $\beta = 2\alpha_y$, the schemes have optimal accuracy and are stable over the time period we examine. Even though the results are not reported here, we have also tested the schemes with the central flux or upwind flux on the element interfaces for \widetilde{E}_z and $\widetilde{\widetilde{E}}_z$ and their arithmetic average for \widehat{E}_z from the four edges connecting to a vertex. We have learned from the numerical experiments that if \widehat{E}_z of the form (38) is used at vertices, it is important to have sufficient numerical dissipation. For instance, \widehat{E}_z based on the multi-dimensional Lax–Friedrichs flux with $\alpha = 2\alpha_x$ and $\beta = 2\alpha_y$ leads to a stable scheme with optimal accuracy, yet \widehat{E}_z based on either the one-dimensional Lax–Friedrichs flux with $\alpha = \alpha_x$ and $\beta = \alpha_y$, or the multi-dimensional HLL flux with $\alpha = 1.2\alpha_x$ and $\beta = 1.2\alpha_y$ leads to unstable schemes due to the insufficiency in numerical dissipation.

4.2 Fourier Analysis of the Scheme with P^0 Approximation

In this subsection, we will carry out the Fourier analysis for the scheme (32)–(33) with P^0 approximation. The goal is to further understand the role of the amount of the numerical dissipation in \widehat{E}_z in the form of (38).

With the P^0 polynomial space, the scheme (32)–(33) becomes

$$\int_{y_{j-\frac{1}{2}}}^{y_{j+\frac{1}{2}}} b_{ij}^x(y) dy = \int_{y_{j-\frac{1}{2}}}^{y_{j+\frac{1}{2}}} B_x^n(x_{i+\frac{1}{2}}, y) dy - \Delta t \left(\widehat{E}_z(x_{i+\frac{1}{2}}, y_{j+\frac{1}{2}}) - \widehat{E}_z(x_{i+\frac{1}{2}}, y_{j-\frac{1}{2}}) \right), \quad (39)$$

$$\int_{x_{i-\frac{1}{2}}}^{x_{i+\frac{1}{2}}} b_{ij}^y(x) dx = \int_{x_{i-\frac{1}{2}}}^{x_{i+\frac{1}{2}}} B_y^n(x, y_{j+\frac{1}{2}}) dx + \Delta t \left(\widehat{E}_z(x_{i+\frac{1}{2}}, y_{j+\frac{1}{2}}) - \widehat{E}_z(x_{i-\frac{1}{2}}, y_{j+\frac{1}{2}}) \right), \quad (40)$$

Table 1 Errors and convergence orders of B_x for the induction equation, with the initial data $(B_x, B_y) = (-\sin(2\pi x), \sin(2\pi y))$ on the domain $\Omega = [0, 1] \times [0, 1]$ and at $t = 1.0, 10.0$. The velocity field is $(u_x, u_y) = (1, 1)$

N	$\alpha = 1, \beta = 1$		$\alpha = 1.2, \beta = 1.2$		$\alpha = 2, \beta = 2$	
	L^2 error	Order	L^2 error	Order	L^2 error	Order
	$t = 1$	$t = 10$	$t = 1$	$t = 10$	$t = 1$	$t = 10$
P^0						
16	1.18E-01	-	2.02E-01	-	3.61E-01	-
32	9.21E-02	0.98	1.06E-01	0.93	2.21E-01	0.71
64	4.69E-02	0.97	5.48E-02	0.95	1.23E-01	0.85
128	2.37E-02	0.98	2.79E-02	0.97	6.49E-02	0.92
256	1.20E-02	0.99	1.41E-02	0.99	3.34E-02	0.96
P^1						
16	1.52E-01	-	6.88E-02	-	6.06E-03	-
32	8.36E-02	0.87	2.16E-04	1.67	1.37E-04	2.14
64	4.37E-02	0.94	5.82E-03	1.89	3.33E-04	2.04
128	2.23E-02	0.97	1.49E-03	1.97	8.25E-05	2.01
256	1.12E-02	0.99	3.75E-04	1.99	2.06E-05	2.00
P^2						
16	9.45E-03	-	7.54E-04	-	1.46E-04	-
32	1.18E-04	3.00	9.44E-05	3.00	1.83E-05	3.00
64	1.47E-05	3.00	1.18E-05	3.00	2.28E-06	3.00
128	1.84E-06	3.00	1.48E-06	3.00	2.86E-07	3.00
256	2.30E-07	3.00	1.85E-07	3.00	3.57E-08	3.00

and the electric field flux \widehat{E}_z at the vertex $(x_{i+\frac{1}{2}}, y_{j+\frac{1}{2}})$ is given by

$$\begin{aligned} \widehat{E}_z(x_{i+\frac{1}{2}}, y_{j+\frac{1}{2}}) &= \frac{1}{4} (E_z |_{I_{ij}} + E_z |_{I_{i+1j}} + E_z |_{I_{ij+1}} + E_z |_{I_{i+1j+1}}) \\ &\quad - \frac{\beta}{4} \left(\frac{B_x |_{I_{ij+1}} + B_x |_{I_{i+1j+1}}}{2} - \frac{B_x |_{I_{ij}} + B_x |_{I_{i+1j}}}{2} \right) \\ &\quad + \frac{\alpha}{4} \left(\frac{B_y |_{I_{i+1j}} + B_y |_{I_{i+1j+1}}}{2} - \frac{B_y |_{I_{ij}} + B_y |_{I_{ij+1}}}{2} \right). \end{aligned} \tag{41}$$

We replace E_z by $u_y B_x - u_x B_y$, and rewrite (41) into

$$\begin{aligned} \widehat{E}_z(x_{i+\frac{1}{2}}, y_{j+\frac{1}{2}}) &= \frac{2u_y - \beta}{8} (B_x |_{I_{ij+1}} + B_x |_{I_{i+1j+1}}) \\ &\quad + \frac{2u_y + \beta}{8} (B_x |_{I_{ij}} + B_x |_{I_{i+1j}}) - \frac{2u_x - \alpha}{8} (B_y |_{I_{i+1j}} + B_y |_{I_{i+1j+1}}) \\ &\quad - \frac{2u_x + \alpha}{8} (B_y |_{I_{ij}} + B_y |_{I_{ij+1}}). \end{aligned} \tag{42}$$

Based on the divergence-free reconstruction procedure, we know $B_x |_{I_{ij}} = B_x |_{I_{i+1j}} = b_{ij}^x$ and $B_y |_{I_{ij}} = B_y |_{I_{ij+1}} = b_{ij}^y$. Therefore (41) is indeed

$$\widehat{E}_z(x_{i+\frac{1}{2}}, y_{j+\frac{1}{2}}) = \frac{2u_y - \beta}{4} b_{ij+1}^x + \frac{2u_y + \beta}{4} b_{ij}^x - \frac{2u_x - \alpha}{4} b_{i+1j}^y - \frac{2u_x + \alpha}{4} b_{ij}^y, \tag{43}$$

and our scheme (39)–(40) can be formulated more explicitly: look for $b_{ij}^{x,n+1}$ and $b_{ij}^{y,n+1}$ in \mathbb{R} , satisfying

$$\begin{aligned} b_{ij}^{x,n+1} &= b_{ij}^{x,n} - \frac{\Delta t}{\Delta y} \left(\frac{2u_y - \beta}{4} (b_{ij+1}^{x,n} - b_{ij}^{x,n}) + \frac{2u_y + \beta}{4} (b_{ij}^{x,n} - b_{ij-1}^{x,n}) \right) \\ &\quad + \frac{\Delta t}{\Delta y} \left(\frac{2u_x - \alpha}{4} (b_{i+1j}^{y,n} - b_{i+1j-1}^{y,n}) + \frac{2u_x + \alpha}{4} (b_{ij}^{y,n} - b_{ij-1}^{y,n}) \right), \end{aligned} \tag{44}$$

$$\begin{aligned} b_{ij}^{y,n+1} &= b_{ij}^{y,n} + \frac{\Delta t}{\Delta x} \left(\frac{2u_y - \beta}{4} (b_{ij+1}^{x,n} - b_{i-1j+1}^{x,n}) + \frac{2u_y + \beta}{4} (b_{ij}^{x,n} - b_{i-1j}^{x,n}) \right) \\ &\quad - \frac{\Delta t}{\Delta x} \left(\frac{2u_x - \alpha}{4} (b_{i+1j}^{y,n} - b_{ij}^{y,n}) + \frac{2u_x + \alpha}{4} (b_{ij}^{y,n} - b_{i-1j}^{y,n}) \right). \end{aligned} \tag{45}$$

Additionally, the divergence-free property of the numerical solution can be translated into the following relation, for any i, j, n ,

$$\Delta y (b_{ij}^{x,n} - b_{i-1j}^{x,n}) + \Delta x (b_{ij}^{y,n} - b_{ij-1}^{y,n}) = 0. \tag{46}$$

The parameters α and β in (41) are taken as

$$\alpha = \sigma |u_x|, \beta = \sigma |u_y|, \tag{47}$$

and σ is a constant that measures the amount of numerical dissipation introduced through the numerical flux \widehat{E}_z . In the next Theorem, we will study the role of this constant σ to the numerical stability of the scheme. The stability condition for $\sigma = 2$ was previously given in [7].

Theorem 4.1 *The scheme (44)–(45) with (46)–(47) is stable under the following condition on the time step size Δt :*

1. When $\sigma \leq 2$,

$$\Delta t \left(\frac{|u_x|}{\Delta x} + \frac{|u_y|}{\Delta y} \right) \leq \frac{\sigma}{2}; \tag{48}$$

2. when $\sigma > 2$

$$\Delta t \left(\frac{|u_x|}{\Delta x} + \frac{|u_y|}{\Delta y} \right) \leq \frac{2}{\sigma}. \tag{49}$$

And the maximum of the upper bound of both formulas is 1, that is, $\max_{\sigma \geq 0} (\frac{\sigma}{2}, \frac{2}{\sigma}) = 1$, and it is attained at $\sigma = 2$.

Proof To carry out the Fourier analysis, let

$$(b^{x,n}, b^{y,n}) = (\widehat{b}_x^n, \widehat{b}_y^n) e^{i(k_1x+k_2y)}, \tag{50}$$

with k_1, k_2 being arbitrary integer. With (50), the Eq. (44) becomes

$$\begin{aligned} \widehat{b}_x^{n+1} = & \widehat{b}_x^n - \frac{\Delta t}{\Delta y} \left(\frac{2u_y - \beta}{4} (e^{ik_2\Delta y} - 1) + \frac{2u_y + \beta}{4} (1 - e^{-ik_2\Delta y}) \right) \widehat{b}_x^n \\ & + \frac{\Delta t}{\Delta y} \left(\frac{2u_x - \alpha}{4} \left(e^{\frac{ik_1\Delta x}{2} + \frac{ik_2\Delta y}{2}} - e^{\frac{ik_1\Delta x}{2} - \frac{ik_2\Delta y}{2}} \right) \right. \\ & \left. + \frac{2u_x + \alpha}{4} \left(e^{-\frac{ik_1\Delta x}{2} + \frac{ik_2\Delta y}{2}} - e^{-\frac{ik_1\Delta x}{2} - \frac{ik_2\Delta y}{2}} \right) \right) \widehat{b}_y^n, \end{aligned} \tag{51}$$

and the divergence-free condition (46) becomes

$$\Delta y \left(e^{\frac{ik_1\Delta x}{2}} - e^{-\frac{ik_1\Delta x}{2}} \right) \widehat{b}_x^n + \Delta x \left(e^{\frac{ik_2\Delta y}{2}} - e^{-\frac{ik_2\Delta y}{2}} \right) \widehat{b}_y^n = 0,$$

i.e.

$$\Delta y \sin \left(\frac{k_1\Delta x}{2} \right) \widehat{b}_x^n + \Delta x \sin \left(\frac{k_2\Delta y}{2} \right) \widehat{b}_y^n = 0. \tag{52}$$

Combining (51) and (52), we get

$$\widehat{b}_x^{n+1} = Q \widehat{b}_x^n, \tag{53}$$

where the amplification factor Q is

$$\begin{aligned} Q = & 1 - \frac{\Delta t}{\Delta y} \left(\frac{2u_y - \beta}{4} (e^{ik_2\Delta y} - 1) + \frac{2u_y + \beta}{4} (1 - e^{-ik_2\Delta y}) \right) \\ & - \frac{\Delta t}{\Delta x} \left(\frac{2u_x - \alpha}{4} e^{\frac{ik_1\Delta x}{2}} + \frac{2u_x + \alpha}{4} e^{-\frac{ik_1\Delta x}{2}} \right) 2i \sin \left(\frac{k_1\Delta x}{2} \right). \end{aligned} \tag{54}$$

One can easily check that (45) and the divergence-free relation (46) will lead to the same amplification factor Q . Without loss of generality, we assume $u_x \geq 0, u_y \geq 0$. Let $c_1 = \frac{\Delta t u_x}{\Delta x}$

and $c_2 = \frac{\Delta t u_y}{\Delta y}$, and with σ defined in (47), we have

$$\begin{aligned}
 Q &= 1 - c_2 \left(\frac{2 - \sigma}{4} (e^{ik_2 \Delta y} - 1) + \frac{2 + \sigma}{4} (1 - e^{-ik_2 \Delta y}) \right) \\
 &\quad - c_1 \left(\frac{2 - \sigma}{4} e^{\frac{ik_1 \Delta x}{2}} + \frac{2 + \sigma}{4} e^{-\frac{ik_1 \Delta x}{2}} \right) 2i \sin \left(\frac{k_1 \Delta x}{2} \right) \\
 &= 1 - \frac{\sigma c_1}{2} (1 - \cos(k_1 \Delta x)) - \frac{\sigma c_2}{2} (1 - \cos(k_2 \Delta y)) \\
 &\quad - i (c_1 \sin(k_1 \Delta x) + c_2 \sin(k_2 \Delta y)).
 \end{aligned} \tag{55}$$

Next, we want to obtain the condition on the time step size to ensure $|Q| \leq 1$. To this end,

$$\begin{aligned}
 |Q|^2 &= \left(1 - \frac{\sigma c_1}{2} (1 - \cos(k_1 \Delta x)) - \frac{\sigma c_2}{2} (1 - \cos(k_2 \Delta y)) \right)^2 \\
 &\quad + (c_1 \sin(k_1 \Delta x) + c_2 \sin(k_2 \Delta y))^2 \\
 &= 1 + \frac{\sigma^2}{4} (c_1 + c_2)^2 + c_1^2 + c_2^2 - \sigma (c_1 + c_2) \\
 &\quad + \frac{\sigma^2}{4} (c_1 \cos(k_1 \Delta x) + c_2 \cos(k_2 \Delta y))^2 - c_1^2 \cos^2(k_1 \Delta x) - c_2^2 \cos^2(k_2 \Delta y) \\
 &\quad + \left(\sigma c_1 - \frac{\sigma^2 c_1^2}{2} - \frac{\sigma^2}{2} c_1 c_2 \right) \cos(k_1 \Delta x) + \left(\sigma c_2 - \frac{\sigma^2 c_2^2}{2} - \frac{\sigma^2}{2} c_1 c_2 \right) \cos(k_2 \Delta y) \\
 &\quad + 2c_1 c_2 \sin(k_1 \Delta x) \sin(k_2 \Delta y).
 \end{aligned} \tag{56}$$

To handle the last term in (56), we will use

$$\begin{aligned}
 \sin(k_1 \Delta x) \sin(k_2 \Delta y) &= \cos(k_1 \Delta x - k_2 \Delta y) - \cos(k_1 \Delta x) \cos(k_2 \Delta y) \\
 &\leq 1 - \cos(k_1 \Delta x) \cos(k_2 \Delta y).
 \end{aligned}$$

Note that this inequality becomes an equality when $k_1 \Delta x = k_2 \Delta y + 2\pi n$ for some $n \in \mathbb{Z}$. Now with $s = \cos(k_1 \Delta x) \in [-1, 1]$ and $t = \cos(k_2 \Delta y) \in [-1, 1]$, (56) turns to

$$\begin{aligned}
 |Q|^2 &\leq 1 + \frac{\sigma^2}{4} (c_1 + c_2)^2 + c_1^2 + c_2^2 - \sigma (c_1 + c_2) + \frac{\sigma^2}{4} (c_1 s + c_2 t)^2 - c_1^2 s^2 - c_2^2 t^2 \\
 &\quad + \frac{\sigma c_1}{2} (2 - \sigma c_1 - \sigma c_2) s + \frac{\sigma c_2}{2} (2 - \sigma c_2 - \sigma c_1) t + 2c_1 c_2 - 2c_1 c_2 s t \\
 &= 1 + \left(\frac{\sigma^2}{4} + 1 \right) (c_1 + c_2)^2 + \left(\frac{\sigma^2}{4} - 1 \right) (c_1 s + c_2 t)^2 \\
 &\quad - \sigma (c_1 + c_2) + \sigma (c_1 s + c_2 t) - \frac{\sigma^2}{2} (c_1 + c_2) (c_1 s + c_2 t).
 \end{aligned} \tag{57}$$

We further set $A = c_1 + c_2$ and $B = c_1 s + c_2 t$, and

$$\begin{aligned}
 |Q|^2 &\leq 1 + \left(\frac{\sigma^2}{4} + 1 \right) A^2 + \left(\frac{\sigma^2}{4} - 1 \right) B^2 - \frac{\sigma^2}{2} AB - \sigma (A - B) \\
 &= 1 + (A - B) \left(\left(\frac{\sigma^2}{4} + 1 \right) A + \left(1 - \frac{\sigma^2}{4} \right) B - \sigma \right).
 \end{aligned}$$

From the definitions of A and B , we know $A - B = c_1(1 - s) + c_2(1 - t) \geq 0$. Hence $|Q|^2 \leq 1$ if

$$\left(\frac{\sigma^2}{4} + 1\right)A + \left(1 - \frac{\sigma^2}{4}\right)B - \sigma \leq 0. \tag{58}$$

There are two cases:

Case 1 When $\sigma \leq 2$, we have $1 - \frac{\sigma^2}{4} \geq 0$. Therefore with $A \geq B$, it is sufficient to require

$$\left(\frac{\sigma^2}{4} + 1\right)A + \left(1 - \frac{\sigma^2}{4}\right)A - \sigma \leq 0,$$

that is, $A \leq \frac{\sigma}{2}$. This can not be further improved, since $A = B$ when $s = t = \cos(k_1 \Delta x) = \cos(k_2 \Delta y) = 1$.

Case 2 When $\sigma > 2$, we have $1 - \frac{\sigma^2}{4} < 0$. Therefore with $A + B = c_1(1 + s) + c_2(1 + t) \geq 0$, it is sufficient to require

$$\left(\frac{\sigma^2}{4} + 1\right)A - \left(1 - \frac{\sigma^2}{4}\right)A - \sigma \leq 0,$$

that is, $A \leq \frac{2}{\sigma}$. Again, this can not be further improved, since $B = -A$ when $s = t = \cos(k_1 \Delta x) = \cos(k_2 \Delta y) = -1$.

In summary,

$$\Delta t \left(\frac{u_x}{\Delta x} + \frac{u_y}{\Delta y} \right) = A \leq \begin{cases} \frac{\sigma}{2}, & \text{if } \sigma \leq 2, \\ \frac{2}{\sigma}, & \text{if } \sigma > 2. \end{cases} \tag{59}$$

Finally one can see the maximum of $\{\sigma/2, 2/\sigma\}$ is 1 when $\sigma = 2$. □

The theorem above implies that the scheme (44)–(45) with the multi-dimensional Lax–Friedrichs numerical flux for \widehat{E}_z , with $\alpha = 2\alpha_x$ and $\beta = 2\alpha_y$, has the largest stability region for our scheme with the P^0 approximation. This is also illustrated by Fig. 2, where comparison is given between the stability regions of the schemes with the multi-dimensional Lax–Friedrichs numerical flux ($\alpha = 2\alpha_x$ and $\beta = 2\alpha_y$) on the right, and one-dimensional Lax–Friedrichs numerical flux ($\alpha = \alpha_x$ and $\beta = \alpha_y$) on the left.

4.3 Our Choices of the Numerical Fluxes in (19)–(21)

Based on the numerical and theoretical studies in previous two subsections for the induction equation, the electric field flux approximations in our proposed schemes (19)–(21) to update the magnetic field in the full ideal MHD simulations will be chosen as follows.

- (1) They satisfy the two conditions in (22)–(23);
- (2) The singled-valued electric field flux \widehat{E}_z at a vertex is determined by the average of the multi-dimensional Lax–Friedrichs numerical fluxes on four edges connecting to this vertex, given by (38) with $\alpha = 2\alpha_x$ and $\beta = 2\alpha_y$;
- (3) On an element interface, the standard one-dimensional Lax–Friedrichs numerical flux (35)–(36) will be applied for both \widetilde{E}_z and $\widetilde{-E}_z$ with parameters α_x and α_y .

Both α_x and α_y in (2) and (3) represent the local speeds of the entire MHD system, and are taken as the largest absolute-value of eigenvalues of the Jacobian $\frac{\partial \mathbf{F}(\mathbf{U}, \mathbf{B}) \cdot \mathbf{n}}{\partial (\mathbf{U}, \mathbf{B})}$, with $\mathbf{n} = (0, 1)^T$, $(1, 0)^T$ respectively, in the neighborhood of the relevant edge. Note that these local speeds are different from that in (37) for the induction equation.

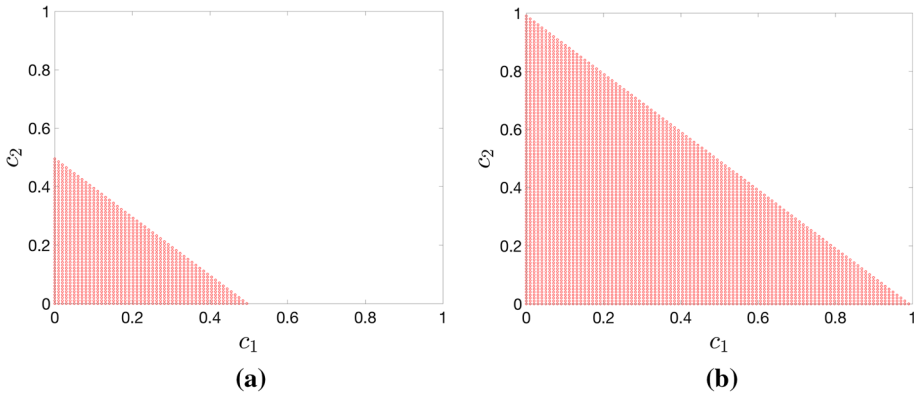


Fig. 2 The stability region of the scheme (32)–(33) for the P^0 approximation with \widehat{E}_z in (38), and $\alpha = \sigma\alpha_x$ and $\beta = \sigma\alpha_y$. Here c_1 is $\frac{\Delta t|u_x|}{\Delta x}$, c_2 is $\frac{\Delta t|u_y|}{\Delta y}$. **a** $\sigma = 1$, **b** $\sigma = 2$

5 Nonlinear Limiter, a Revisit to the Reconstruction

In this section, we will discuss the use of nonlinear limiters to enhance numerical stability of the proposed schemes. Similar to high order DG methods for nonlinear hyperbolic conservation laws, nonlinear limiters are also needed for numerical stability of our methods. In this paper, the *minmod* total variation bounded (TVB) slope limiter in [16] is applied. This limiter involves a non-negative parameter M , and its value is often chosen for each example in actual implementation [14,31]. This limiter can be applied to component-wise variables or in local characteristic fields with respect to the 7×7 -eigen system in [23].

Following the work in [26,27] with globally divergence-free central DG methods, for non-smooth solutions, we first apply the limiter only to the hydrodynamic variables \mathbf{U}_h , not to $\mathcal{B}_h, \widetilde{\mathcal{B}}_h$ or (b_{ij}^x, b_{ij}^y) . This works well for the schemes with P^1 approximations, and when the discontinuities in the solutions are not strong.

It is known that central type schemes are in general more dissipative hence more stable than upwind type schemes. Therefore it is not unexpected that when our proposed DG methods are used to examples with strong shocks, it seems necessary to apply the nonlinear limiter to both \mathbf{U}_h and the magnetic field \mathcal{B}_h in order to effectively control numerical oscillations. One needs to be careful, though, about how to implement this without losing the globally divergence-free property of the computed magnetic field. A straightforward implementation will break the intrinsic relation between the data $\widetilde{\mathcal{B}}_h$ and (b_{ij}^x, b_{ij}^y) used in the reconstruction (see the proof of Theorem 3.1). On the other hand, for the methods we will focus on in this paper with P^1 and P^2 approximations, an alternative but equivalent way was presented in [27] to reconstruct I_{ij} , look for $\mathcal{B}_h^{n+1} \in \mathcal{W}^k(I_{ij})$ such that

1. $B_x^{n+1}(x_{l+\frac{1}{2}}, y) = b_{lj}^x(y)$ for $l = i - 1, i$ and $y \in [y_{j-\frac{1}{2}}, y_{j+\frac{1}{2}}]$,
2. $B_y^{n+1}(x, y_{l+\frac{1}{2}}) = b_{il}^y(x)$ for $l = j - 1, j$ and $x \in [x_{i-\frac{1}{2}}, x_{i+\frac{1}{2}}]$,
3. $\nabla \cdot \mathcal{B}_h^{n+1}|_{I_{ij}} = 0$.

One can refer to [26] for the proof of the equivalency. An important feature of this equivalent reconstruction is that only the interface data (b_{ij}^x, b_{ij}^y) is needed. Now when the nonlinear limiter needs to be applied to the magnetic field, the normal components of the magnetic field $\{b_{ij}^x\}_{ij}, \{b_{ij}^y\}_{ij}$ will be limited first (this will be discussed in details next), then the equivalent

reconstruction given above will be used to obtain the globally divergence-free magnetic field based on the limited normal components of the magnetic field.

We here will use $k = 2$ as an example to illustrate how to apply the *minmod* TVB limiter to $\{b_{ij}^x\}_{ij}$ and $\{b_{ij}^y\}_{ij}$. The quadratic polynomial b_{ij}^x can be written as

$$b_{ij}^x(y) = \overline{b_{ij}^x} + c_y Y + c_{yy} \left(Y^2 - \frac{1}{3} \right), \tag{60}$$

with $Y = \frac{y-y_j}{\Delta y/2}$, and $\overline{b_{ij}^x}$ is the edge average of b_{ij}^x , namely,

$$\overline{b_{ij}^x} = \frac{1}{\Delta y} \int_{y_{j-\frac{1}{2}}}^{y_{j+\frac{1}{2}}} b_{ij}^x(y) dy. \tag{61}$$

We compute \tilde{c}_y according to

$$\tilde{c}_y = \tilde{m} \left(c_y, \Delta_+ \overline{b_{ij}^x}, \Delta_- \overline{b_{ij}^x} \right). \tag{62}$$

Here $\Delta_+ \overline{b_{ij}^x} = \overline{b_{ij+1}^x} - \overline{b_{ij}^x}$, $\Delta_- \overline{b_{ij}^x} = \overline{b_{ij}^x} - \overline{b_{ij-1}^x}$, and the corrected *minmod* TVB function \tilde{m} is

$$\tilde{m}(a_1, a_2, a_3) = \begin{cases} a_1, & \text{if } |a_1| \leq M(\Delta y)^2; \\ m(a_1, a_2, a_3), & \text{otherwise,} \end{cases} \tag{63}$$

with the *minmod* function m defined as

$$m(a_1, a_2, a_3) = \begin{cases} s \min(|a_1|, |a_2|, |a_3|), & \text{if } s = \text{sign}(a_1) = \text{sign}(a_2) = \text{sign}(a_3); \\ 0, & \text{otherwise.} \end{cases} \tag{64}$$

If $|\tilde{c}_y - c_y| > 10^{-6}$, we apply the limiter by setting $c_y = \tilde{c}_y$ and $c_{yy} = 0$ in (60). Otherwise, no modification is made to (60). The treatment for b_{ij}^y is very similar. It is important to know that the limiter does not change the edge averages $\{b_{ij}^x\}_{ij}$ and $\{b_{ij}^y\}_{ij}$, hence a necessary compatible condition for the exactly divergence-free reconstruction, namely,

$$\int_{I_{ij}} \nabla \cdot \mathcal{B}_h^n dx dy = \Delta y \left(\overline{b_{ij}^{x,n}} - \overline{b_{i-1,j}^{x,n}} \right) + \Delta x \left(\overline{b_{ij}^{y,n}} - \overline{b_{ij,-1}^{y,n}} \right) = 0 \tag{65}$$

still holds.

Finally in Algorithm 1, we provide the flow chart of the proposed globally divergence-free methods when they are applied to ideal MHD equations. The time discretization is taken to be the forward Euler method.

6 Numerical Results

In this section, numerical examples are presented to illustrate the accuracy and stability of the proposed globally divergence-free methods with P^1 and P^2 approximations for the ideal MHD equations. They include two smooth examples and five non-smooth examples. In our simulations, uniform rectangular meshes with $N \times N$ elements are used. The initial numerical solution $\mathbf{U}_h \in \mathcal{V}_h^k$ is obtained through the L^2 projection, and $\mathcal{B}_h \in \mathcal{M}_h^k$ is by the BDM projection [10]. In time, a third order TVD Runge–Kutta method is applied [21].

Algorithm 1 The algorithm of the globally divergence-free DG methods for ideal MHD equations, with the forward Euler method as the time discretization.

Initialization:

Initialize \mathbf{U}_h^0 via the L^2 projection and \mathcal{B}_h^0 via the BDM projection. If the example is non-smooth, apply the TVB limiter to \mathbf{U}_h^0 .

Time evolution:

With the numerical solutions available at time t_n for $n \geq 0$, namely $(\mathbf{U}_h^n, \mathcal{B}_h^n) \in \mathcal{V}_h^k \times \mathcal{M}_h^k$ with $\mathcal{B}_h^n = (B_{x,h}^n, B_{y,h}^n)^T$, update $(\mathbf{U}_h^{n+1}, \mathcal{B}_h^{n+1}) \in \mathcal{V}_h^k \times \mathcal{M}_h^k$ with $\mathcal{B}_h^{n+1} = (B_{x,h}^{n+1}, B_{y,h}^{n+1})^T$ at $t_{n+1} = t_n + \Delta t$;

- 1: Compute the time step Δt based on the maximum value α_x, α_y ;
- 2: Impose boundary conditions;
- 3: Pre-compute the numerical solutions at t_{n+1} :
 - for each element I_{ij} , update \mathbf{U}_h^{n+1} by scheme (14);
 - for each y -direction element interface, compute $\{b_{ij}^x\}_{ij}$ by scheme (19);
 - for each x -direction element interface, compute $\{b_{ij}^y\}_{ij}$ by scheme (20);
 - if $k \geq 2$, compute $\tilde{\mathcal{B}}_h$ on each element I_{ij} by scheme (21);
- 4: If the example is non-smooth, apply the TVB limiter to \mathbf{U}_h^{n+1} ; for challenging non-smooth examples (such as the cloud–shock example), also apply the limiter as in Sect. 5 to $\{b_{ij}^x\}_{ij}$ and $\{b_{ij}^y\}_{ij}$;
- 5: Reconstruction on each element: if the limiter is not applied to $\{b_{ij}^x\}_{ij}$ and $\{b_{ij}^y\}_{ij}$, reconstruct \mathcal{B}_h^{n+1} following **R1–R3** in Sect. 3.2.3; otherwise, reconstruct \mathcal{B}_h^{n+1} following the procedure given in Sect. 5;
- 6: Return $(\mathbf{U}_h^{n+1}, \mathcal{B}_h^{n+1}) \in \mathcal{V}_h^k \times \mathcal{M}_h^k$.

That is, to solve $u_t = L(u, t)$, given the numerical solution u^n at t_n , we compute u^{n+1} at $t_{n+1} = t_n + \Delta t$ as follows,

$$\begin{aligned}
 u^{(1)} &= u^n + \Delta t L(u_n, t_n), \\
 u^{(2)} &= \frac{3}{4}u^n + \frac{1}{4}u^{(1)} + \frac{1}{4}\Delta t L\left(u^{(1)}, t_n + \Delta t\right), \\
 u^{n+1} &= \frac{1}{3}u^n + \frac{2}{3}u^{(2)} + \frac{2}{3}\Delta t L\left(u^{(2)}, t_n + \frac{1}{2}\Delta t\right).
 \end{aligned}
 \tag{66}$$

The time step is determined by

$$\Delta t = \frac{CFL}{\alpha_x/\Delta x + \alpha_y/\Delta y},
 \tag{67}$$

where α_x and α_y are the largest absolute eigenvalues of Jacobian $\frac{\partial F_1(\mathbf{U}, \mathcal{B})}{\partial(\mathbf{U}, \mathcal{B})}$ and $\frac{\partial F_2(\mathbf{U}, \mathcal{B})}{\partial(\mathbf{U}, \mathcal{B})}$, respectively. We take $CFL = 0.2$ for $k = 1$ and $CFL = 0.1$ for $k = 2$ similar as for the standard DG methods. The numerical fluxes in the schemes to update the magnetic field follow the strategies summarized in Sect. 4.3. The *minmod* TVB slope limiter is applied for non-smooth examples with $M = 1$.

6.1 Smooth Examples

6.1.1 The Smooth Vortex Problem

The first example we consider is the smooth vortex example which was introduced in [2], and it models a smooth vortex propagating with speed (1, 1) in a two-dimensional domain. The initial condition is given by

$$(\rho, u_x, u_y, u_z, B_x, B_y, B_z, p) = (1, 1 + \delta u_x, 1 + \delta u_y, 0, \delta B_x, \delta B_y, 0, 1 + \delta p),$$

Table 2 L^2 errors and orders of accuracy of ρ , u_x , B_x and p for smooth vortex problem at $t = 20$. The computational domain is $[-10, 10] \times [-10, 10]$

N	ρ		u_x		p		B_x	
	L^2 error	Order	L^2 error	Order	L^2 error	Order	L^2 error	Order
p^1								
32	3.98E-05	–	9.18E-03	–	1.22E-03	–	7.51E-03	–
64	2.44E-05	0.71	3.45E-03	1.41	5.44E-04	1.17	2.75E-03	1.45
128	8.23E-06	1.58	6.80E-04	2.34	1.20E-04	2.19	5.35E-04	2.36
256	1.84E-06	2.16	9.45E-05	2.85	1.98E-05	2.60	7.39E-05	2.87
p^2								
32	1.50E-04	–	1.96E-03	–	1.02E-03	–	7.10E-03	–
64	6.62E-05	1.18	8.76E-04	1.16	4.90E-04	1.06	2.56E-03	1.47
128	1.30E-05	2.35	1.70E-04	2.37	9.76E-05	2.33	4.63E-04	2.47
256	1.76E-06	2.88	2.31E-05	2.88	1.33E-05	2.87	6.21E-05	2.90

where

$$\begin{aligned}
 (\delta u_x, \delta u_y) &= \frac{\xi}{2\pi} \widehat{\nabla} \times \exp\{0.5(1 - r^2)\}, \quad (\delta B_x, \delta B_y) = \frac{\eta}{2\pi} \widehat{\nabla} \times \exp\{0.5(1 - r^2)\}, \\
 \delta p &= \frac{\eta^2(1 - r^2 - \xi^2)}{8\pi^2} \exp(1 - r^2).
 \end{aligned}$$

Here $r = \sqrt{x^2 + y^2}$, $\xi = \eta = 1$ and $\gamma = 5/3$. The computational domain is taken as $[-10, 10] \times [-10, 10]$. Even though the problem is not-periodic, periodic boundary conditions are used in our simulation. This will introduce an error of size $O(10^{-22})$ which is negligible with respect to the resolution of the numerical solutions. In Table 2, L^2 errors and orders of accuracy are presented for the variables ρ , u_x , B_x and pressure p at $t = 20$, right after one time period, by which the vortex returns to its initial location. The results show that our numerical schemes have $(k + 1)$ th order accuracy for $k = 1, 2$. For this smooth example, no nonlinear limiter is needed.

6.1.2 The Smooth Alfvén Wave

The second smooth example is the smooth Alfvén wave problem, which describes a circularly polarized Alfvén wave moving in the domain $\Omega = [0, 1/\cos \alpha] \times [0, 1/\sin \alpha]$ [28, 37]. Here, α represents the angle of the wave propagation with respect to x -axis, and it is set to be $\pi/4$. The same initial data as in [28] is taken

$$\begin{aligned}
 \rho &= 1, u_{\parallel} = 0, u_{\perp} = 0.1 \sin(2\pi\beta), u_z = 0.1 \cos(2\pi\beta), \\
 B_{\parallel} &= 1, B_{\perp} = u_{\perp}, B_z = u_z, p = 0.1,
 \end{aligned}$$

where $\beta = x \cos \alpha + y \sin \alpha$. The subscripts \parallel and \perp denote the directions parallel and perpendicular to the wave propagation direction, respectively. Periodic boundary conditions are used and $\gamma = 5/3$. The Alfvén wave travels at a constant Alfvén speed $B_{\parallel}/\sqrt{\rho} = 1$. The solution returns to its initial configuration when time t is an integer. In Table 3, we present the L^2 errors and orders of accuracy for u_x , u_z , B_x and p at time $t = 2$. From the results, we can see that the P^k approximations with $k = 1, 2$ are $(k + 1)$ th order accurate, and they are optimal. No nonlinear limiter is applied.

Table 3 L^2 errors and orders of accuracy for u_x, u_z, p and B_x for smooth Alfvén wave problem at $t = 2$. The computational domain is $[0, \sqrt{2}] \times [0, \sqrt{2}]$

N	u_x		u_z		p		B_x	
	L^2 error	order	L^2 error	order	L^2 error	order	L^2 error	order
p^1								
16	2.99E-03	–	3.91E-03	–	7.41E-04	–	2.44E-03	–
32	4.27E-04	2.81	5.69E-04	2.78	1.14E-04	2.71	3.35E-04	2.87
64	6.82E-05	2.65	9.47E-05	2.59	1.96E-05	2.54	4.87E-05	2.78
128	1.34E-05	2.34	1.94E-05	2.29	4.10E-06	2.25	8.59E-06	2.50
p^2								
16	3.88E-03	–	7.17E-04	–	3.64E-03	–	2.08E-03	–
32	3.50E-04	3.47	5.38E-05	3.73	3.27E-04	3.48	2.01E-04	3.37
64	2.56E-05	3.78	2.81E-06	4.26	1.71E-05	4.26	1.78E-05	3.50
128	2.81E-06	3.19	2.36E-07	3.57	1.39E-06	3.62	2.09E-06	3.09

6.2 Non-smooth Examples

6.2.1 The Field Loop Advection

In this subsection, we consider the magnetic field loop advection problem originally introduced in [20]. The same initial data as in [27] is taken, with $(\rho, u_x, u_y, u_z, B_z, p) = (1, 2, 1, 1, 0, 1)$, and $(B_x, B_y) = \widehat{\nabla} \times A_z$. Here A_z is the z -component of the magnetic potential

$$A_z = \begin{cases} A_0(R - r) & \text{if } r \leq R, \\ 0 & \text{if } r > R, \end{cases}$$

with $A_0 = 10^{-3}$, $R = 0.3$ and $r = \sqrt{x^2 + y^2}$. This problem is computed on the domain $[-1, 1] \times [-0.5, 0.5]$ with a 200×100 mesh. Periodic boundary conditions are used and $\gamma = 5/3$.

In Fig. 3, we report the gray-scale images of the magnetic pressure $B_x^2 + B_y^2$ (left) and the magnetic field lines (right) at time $t = 0, t = 2$ and $t = 10$. With the globally divergence-free magnetic field, the magnetic field lines are plotted by contouring the z -component of the numerical magnetic potential A_z . The magnetic pressure is convected across the domain periodically, and this is confirmed by our numerical results based on P^2 approximation. The component-wise *minmod* TVB limiter is applied to \mathbf{U}_h with the parameter $M = 1$. There is no visible difference in the numerical results when the limiter is applied to the local characteristic fields. Overall our schemes capture the field loop well. From the images on the left in Fig. 3, one can observe numerical dissipation around the center and the boundary of the loop, similar to the observation in [20, 26, 27]. There is no obvious oscillations in our solutions even at later time $t = 10$ unlike in some numerical results commented in [20, 28]. From the images on the right of Fig. 3, symmetry can be seen in the magnetic field lines, with some distortion at $t = 10$ due to the accumulated numerical dissipation over long time simulation.

Note that the initial data is discontinuous, and one needs to pay special attention to the initialization to ensure the magnetic field being divergence-free at $t = 0$. For example,

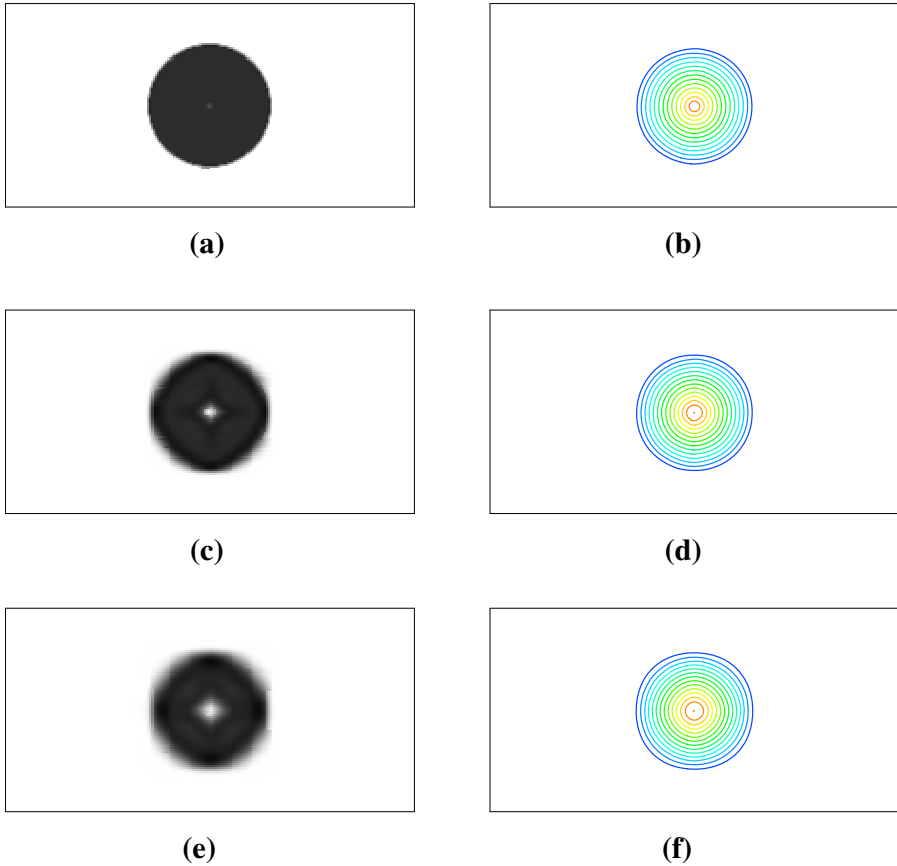


Fig. 3 The magnetic pressure $B_x^2 + B_y^2$ (left) and magnetic field lines (right) of the field loop advection. P^2 approximation on 200×100 mesh. The magnetic field lines are plotted with the same range. **a** Magnetic pressure at $t = 0$, **b** magnetic field lines at $t = 0$, **c** magnetic pressure at $t = 2$, **d** magnetic field lines at $t = 2$, **e** magnetic pressure at $t = 10$, **f** magnetic field lines at $t = 10$

to apply the BDM projection to the initial magnetic field, one needs to compute the first order coefficient $B_x^0 := \frac{1}{\Delta x \Delta y} \int_{I_{ij}} B_x dx dy$ with $B_x = \partial A_z / \partial y$. If a numerical quadrature is applied without taking into account the discontinuity in B_x , then nonzero divergence will be introduced to the magnetic field approximation. Instead, we will evaluate B_x^0 as follows,

$$B_x^0 = \frac{1}{\Delta x \Delta y} \int_{I_{ij}} \frac{\partial A_z}{\partial y} dx dy = \frac{1}{\Delta x \Delta y} \int_{x_{i-\frac{1}{2}}}^{x_{i+\frac{1}{2}}} [A_z(x, y_{j+\frac{1}{2}}) - A_z(x, y_{j-\frac{1}{2}})] dx. \quad (68)$$

Similarly, to evaluate $a_{0R} := \frac{1}{\Delta y} \int_{y_{j-\frac{1}{2}}}^{y_{j+\frac{1}{2}}} B_x(x_{i+\frac{1}{2}}, y) dy$, we will follow

$$a_{0R} = \frac{1}{\Delta y} \int_{y_{j-\frac{1}{2}}}^{y_{j+\frac{1}{2}}} \frac{\partial A_z}{\partial y} dy = \frac{1}{\Delta y} (A_z(x_{i+\frac{1}{2}}, y_{j+\frac{1}{2}}) - A_z(x_{i+\frac{1}{2}}, y_{j-\frac{1}{2}})). \quad (69)$$

This will lead to an exactly divergence-free magnetic field approximation at $t = 0$.

6.2.2 Orszag–Tang Vortex Problem

In this subsection, we test the Orszag–Tang vortex problem, whose solution involves the formation and interaction of multiple shocks as the nonlinear system evolves in time. The same initial data as in [25] is taken, namely,

$$\begin{aligned} \rho &= \gamma^2, & u_x &= -\sin y, & u_y &= \sin x, & u_z &= 0, \\ B_x &= -\sin y, & B_y &= \sin 2x, & B_z &= 0, & p &= \gamma. \end{aligned}$$

This problem is computed on the domain $[0, 2\pi] \times [0, 2\pi]$ with a 192×192 mesh based on P^1 and P^2 approximations. Periodic boundary conditions are used with $\gamma = 5/3$. Figures 4 and 5 demonstrate the time evolutions of the density ρ at times $t = 3, 4$ with P^1 and P^2 approximations, respectively. The component-wise *minmod* TVB limiter is applied to \mathbf{U}_h with the parameter $M = 1$. The results show that our schemes work well for this problem and they are in good agreement with the results in literature [23, 25, 27].

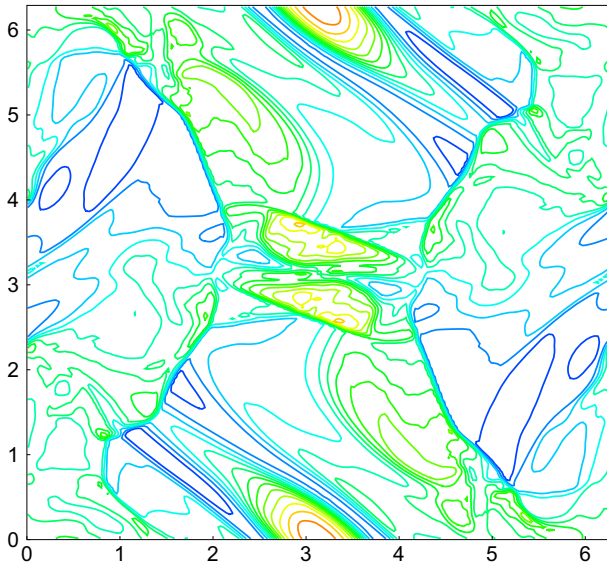
As observed in [23, 25, 29], different numerical methods can demonstrate different levels of stability for this example, (partially) depending on their ability to control the divergence error in the computed magnetic field. Standard numerical methods that work well for nonlinear hyperbolic conservation laws can show instability when simulating this example, if the divergence error is not sufficiently controlled. Our proposed exactly divergence-free DG methods display very good stability over long time simulation, for example the schemes with P^1 and P^2 approximations are stable up to $t = 25$ (the maximum time we run) on the 192×192 mesh when the *minmod* TVB limiter is applied in local characteristic fields. In addition to the divergence error, as indicated in [37] the choices of the limiters can also affect the numerical stability. When the component-wise *minmod* TVB limiter is applied, the simulation will break down at $t = 7.4$ with the P^2 approximation. Again, the limiters are only applied to \mathbf{U}_h .

For this example, we further perform a convergence study for the methods with P^2 approximation. In Fig. 6, we plot the pressure p (left) at $y = 1.99635$ and $t = 2$, and the magnetic variable B_x at $x = \pi$ and $t = 3$, computed with the 192×192 (circle) and 384×384 (line) meshes. With shocks developed in the solution, convergence is observed. The pressure lines and magnetic field lines are comparable to the results by the locally divergence-free DG methods in [25] and exactly divergence-free central DG methods in [26, 27]. As in [26, 27], there is no negative pressure produced throughout the simulation.

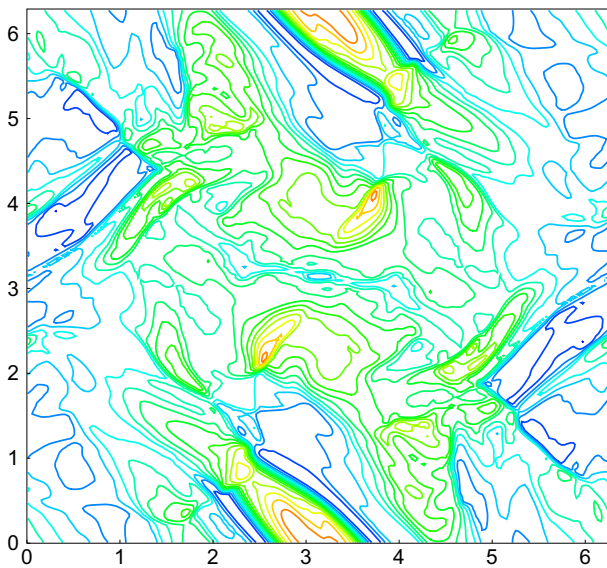
6.2.3 The Rotor Problem

In this subsection, a rotor problem is considered which was first documented in [8]. This problem describes a dense disk of fluid rapidly spinning in a light ambient fluid. To reduce the initial transition, a “taper” function is used to bridge these two areas. We take the same initial data as in [26, 37], that is,

$$(u_z, B_x, B_y, B_z, p) = \left(0, 2.5/\sqrt{4\pi}, 0, 0, 0.5\right),$$



(a)



(b)

Fig. 4 Development of the density ρ in Orszag–Tang vortex problem with P^1 approximation at $t = 3$, $t = 4$ on 192×192 mesh. 15 equally spaced contours with ranges $[1.144, 6.134]$, $[1.179, 5.813]$ respectively. **a** $t = 3$, **b** $t = 4$

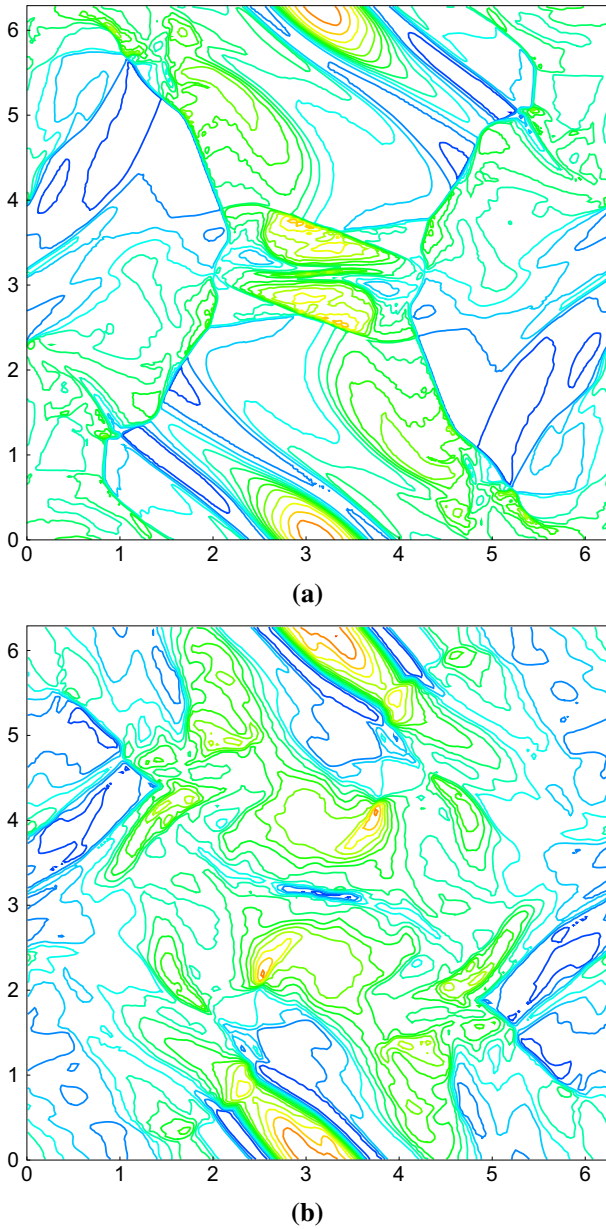


Fig. 5 Development of the density ρ in the Orszag–Tang vortex problem with P^2 approximation at $t = 3$, $t = 4$ on 192×192 mesh. 15 equally spaced contours with ranges $[1.122, 6.161]$, $[1.127, 5.857]$, respectively. **a** $t = 3$, **b** $t = 4$

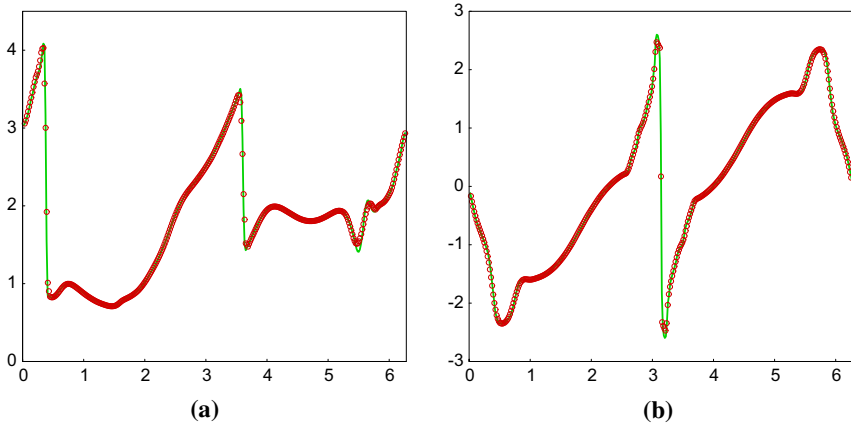


Fig. 6 The P^2 approximation for the Orszag–Tang vortex problem on 192×192 (circle) and 384×384 (solid line) meshes. **a** p with $y = 1.9635$ at $t = 2$, **b** B_x with $x = \pi$ at $t = 3$

and

$$(\rho, u_x, u_y) = \begin{cases} (10, -(y - 0.5)/r_0, (x - 0.5)/r_0) & r < r_0 \\ (1 + 9\lambda, -\lambda(y - 0.5)/r, \lambda(x - 0.5)/r) & r_0 < r < r_1 \\ (1, 0, 0) & r > r_1 \end{cases}$$

where $r = \sqrt{(x - 0.5)^2 + (y - 0.5)^2}$, $r_0 = 0.1$, $r_1 = 0.115$ and $\lambda = (r_1 - r)/(r_1 - r_0)$. We simulate the problem in the domain $[0, 1] \times [0, 1]$. Periodic boundary conditions are used and $\gamma = 5/3$.

In Figs. 7 and 8, we present the results of density ρ , pressure p , the hydrodynamic Mach number $|\mathbf{u}|/c$ with the sound speed $c = \sqrt{\gamma p/\rho}$, and the magnetic pressure $|\mathbf{B}|^2/2$ at $t = 0.295$, based on P^1 and P^2 approximations on the 200×200 mesh. The *minmod* TVB limiter is applied in the characteristic fields and only to \mathbf{U}_h . Compared with the results in [25, 37], our methods also resolve this problem well. When divergence error is not sufficiently controlled in the magnetic field by some numerical methods, “distortion” can develop in Mach number [25, 37]. In Fig. 9, we zoom in the central part of the Mach number, and no “distortion” is observed.

As in [26, 27], we examine the convergence of the methods with P^2 approximation. In Fig. 10, we present the Mach number with $x = 0.413$ (left) and the magnetic field B_x (right) with $x = 0.25$ at $t = 0.295$ on 400×400 (circle) and 600×600 (solid) meshes. Convergence of the method is observed, with the shocks being captured in the numerical solution. The cut lines in Fig. 10 are very close to the results in [26], and there is no significant oscillation in the solutions. In our simulation, negative pressure is not observed.

6.2.4 The Blast Problem

In this subsection, we consider the blast problem as in [8]. There are strong magnetosonic shocks in the solution. The initial condition is taken as

$$(\rho, u_x, u_y, u_z, B_x, B_y, B_z, p) = \begin{cases} (1, 0, 0, 0, \frac{100}{\sqrt{4\pi}}, 0, 0, 1000), & r \leq R, \\ (1, 0, 0, 0, \frac{100}{\sqrt{4\pi}}, 0, 0, 0.10), & r > R, \end{cases}$$

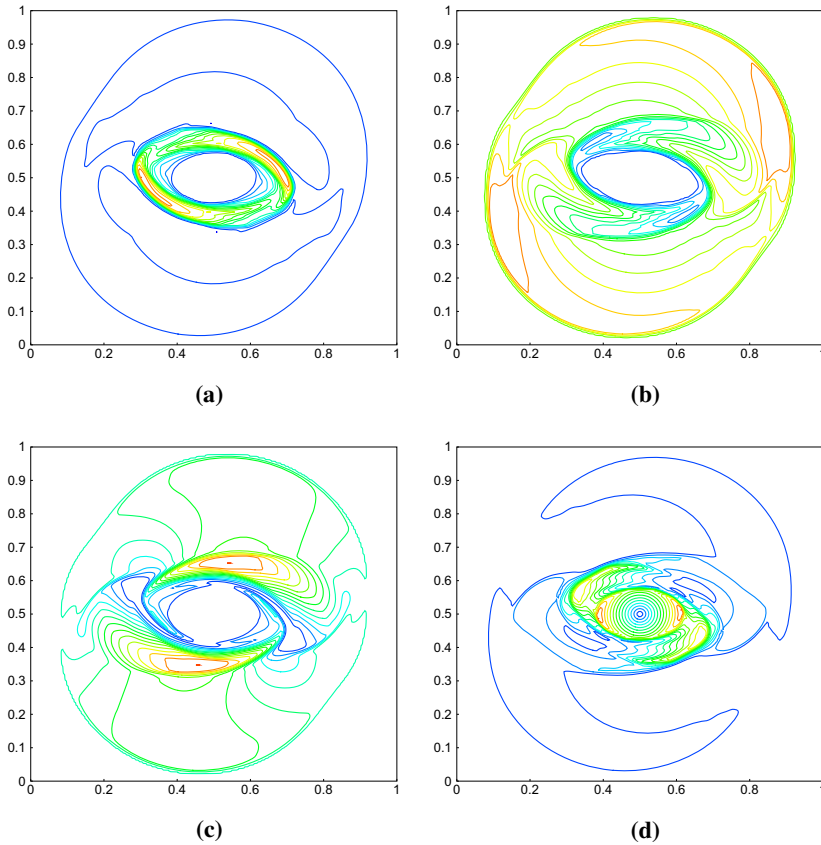


Fig. 7 P^1 approximation for the rotor problem on the 200×200 mesh at $t = 0.295$. 15 equally spaced contours. **a** $\rho \in [0.507, 8.837]$, **b** $p \in [0.010, 0.774]$, **c** $|B|^2/2 \in [0.012, 0.676]$, **d** $|u|/c \in [0, 2.673]$

with $r = \sqrt{x^2 + y^2}$ and $R = 0.1$. With this setup, the fluid pulse has very small plasma beta, namely, $\beta = \frac{p}{(B_x^2 + B_y^2)/2} = 2.513E-04$, in the region outside the initial pressure pulse. We carry out the simulation in the domain $[-0.5, 0.5] \times [-0.5, 0.5]$ with a 200×200 mesh. Outgoing boundary conditions are used and $\gamma = 1.4$.

In Figs. 11 and 12, we report the numerical results at time $t = 0.01$ based on P^1 and P^2 approximations for density ρ , pressure p , square of total velocity $u_x^2 + u_y^2$, and the magnetic pressure $B_x^2 + B_y^2$, respectively. As pointed out in [8, 26–28], this is a stringent problem to solve. In our simulation, negative pressure is observed near the shock front, similar as in many other methods when positivity preserving techniques are not applied to pressure [26–28]. In Fig. 13, we plot the negative part of pressure, $\min(0, p)$, based on the P^1 and P^2 approximations. The minimum of pressure in the P^2 approximation is -16.295 , and it is more negative than -4.369 , the minimum of the pressure in the P^1 approximation. These results are obtained when the component-wise *minmod* TVB limiter is applied only to \mathbf{U}_h .

To further improve the numerical stability, we run the simulation by applying the *minmod* TVB limiter to both the hydrodynamic variables \mathbf{U}_h and the normal component of the magnetic field $\{b_{ij}^x\}_{ij}$ and $\{b_{ij}^y\}_{ij}$ (see Sect. 5 for details of the limiter and the reconstruction). In

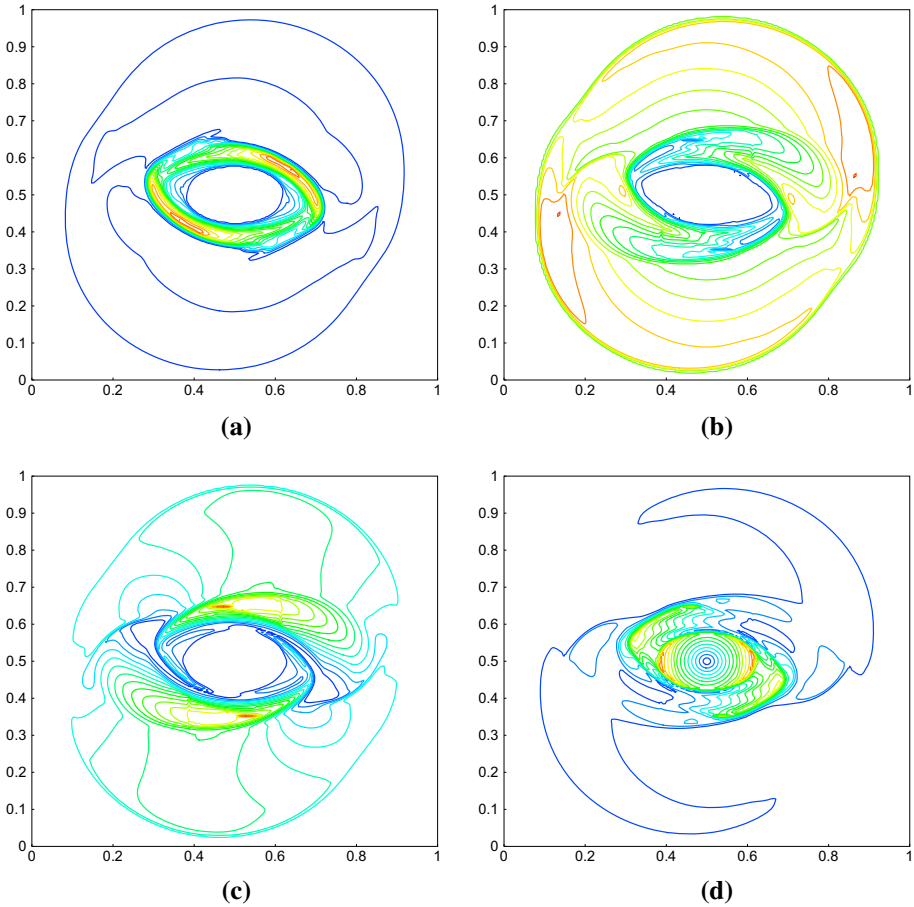


Fig. 8 P^2 approximation for the rotor problem on the 200×200 mesh at $t = 0.295$. 15 equally spaced contours. **a** $\rho \in [0.551, 9.910]$, **b** $p \in [0.008, 0.776]$, **c** $|\mathbf{B}|^2/2 \in [0.012, 0.847]$, **d** $|\mathbf{u}|/c \in [0, 3.033]$

Fig. 14, the results are shown for density ρ , pressure p , square of total velocity $u_x^2 + u_y^2$, and the magnetic pressure $B_x^2 + B_y^2$, respectively, at $t = 0.01$ based on P^2 approximation. With the magnetic field being limited, the minimum of pressure is now -7.347 which is greatly improved, hence the schemes with all unknowns being limited are more robust.

Remark 6.1 Following Zhang and Shu’s important work in [41] to design positivity-preserving limiters for high order numerical methods, similar limiters were developed in [12] for DG and central DG methods to simulate ideal MHD equations. Locally divergence-free approximations can be easily used for the methods in [12] without affecting the positivity-preserving property of the overall algorithms. Unfortunately, such limiters can not be applied to the proposed methods in this paper, as they will destroy the globally divergence-free property of the numerical solutions.

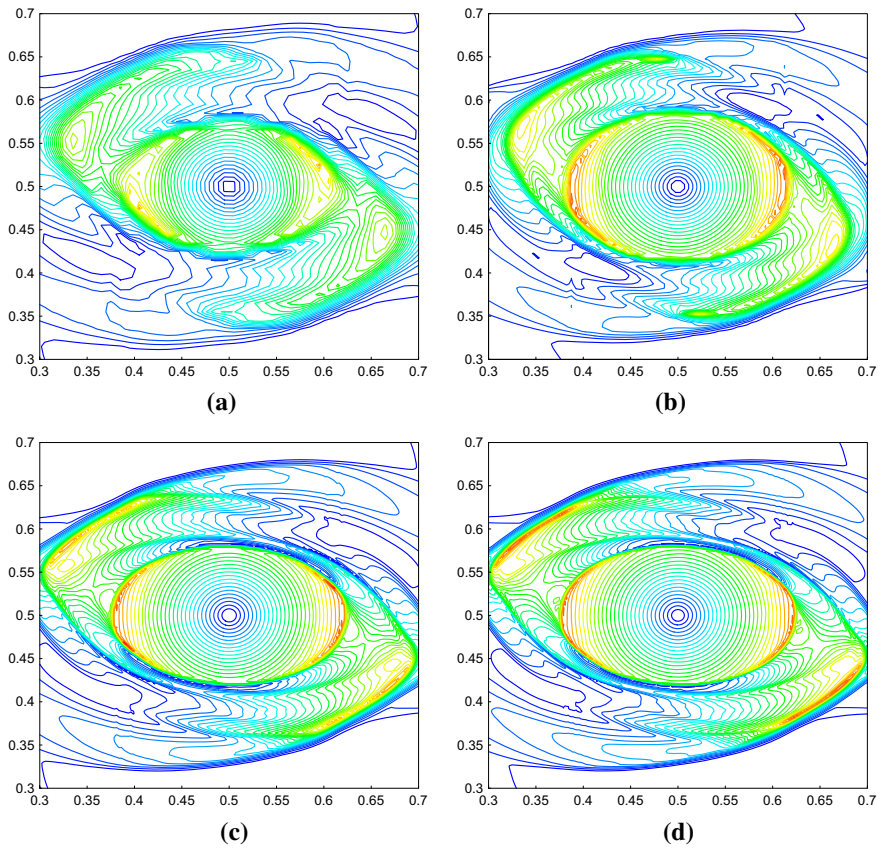


Fig. 9 Zoom-in central part of Mach number $|u|/c$ with P^2 approximation in the rotor problem at $t = 0.295$. 30 equally spaced contours with range $[0.18, 3.12]$. **a** 100×100 mesh, **b** 200×200 mesh, **c** 400×400 mesh, **d** 600×600 mesh

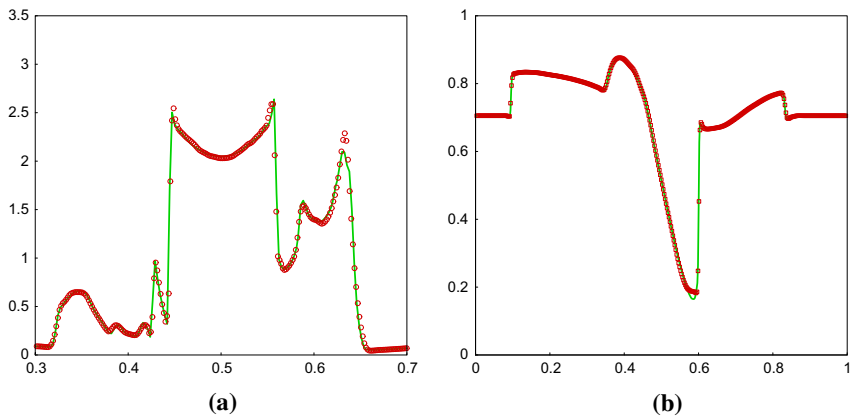


Fig. 10 The Mach number $|u|/c$ and magnetic field B_x of the rotor problem with P^2 approximation at $t = 0.295$ on 400×400 (circle) and 600×600 (solid line) meshes. **a** $|u|/c$ with $x = 0.41$, **b** B_x with $x = 0.25$

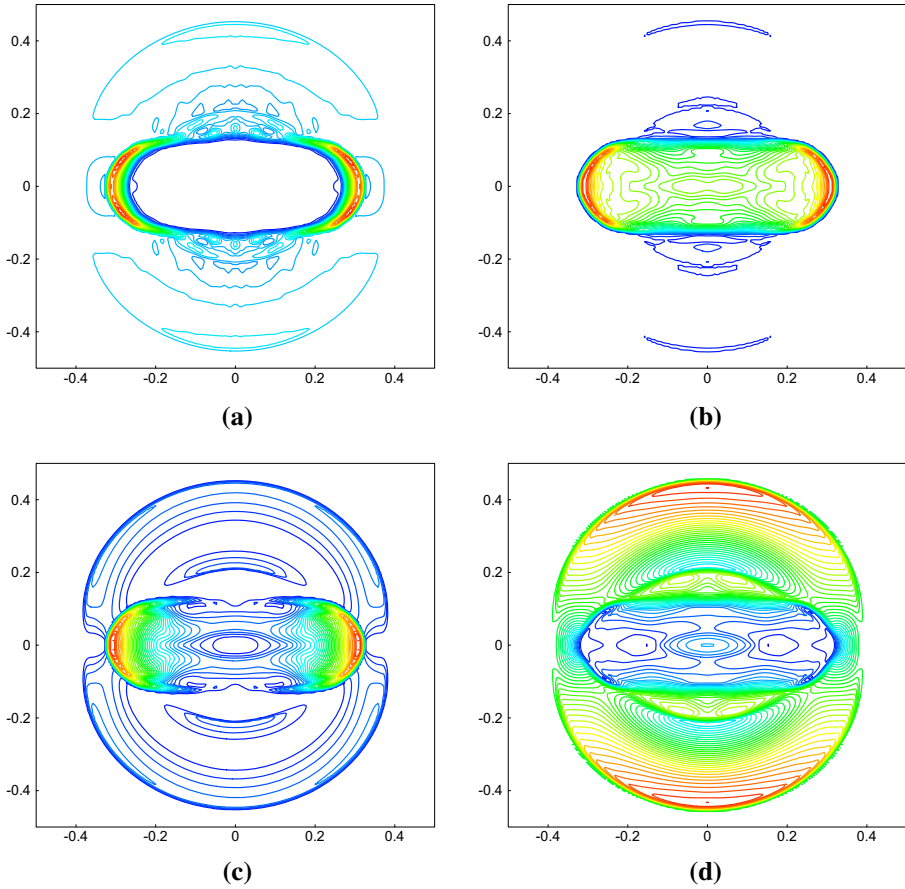


Fig. 11 P^1 approximation for the blast problem on the 200×200 mesh at $t = 0.01$. 40 equally spaced contours are plotted. **a** $\rho \in [0.184, 4.602]$, **b** $p \in [-4.369, 259.297]$, **c** $u_x^2 + u_y^2 \in [0, 288.251]$, **d** $B_x^2 + B_y^2 \in [431.002, 1186.060]$

6.2.5 The Cloud–Shock Interaction

The last example we consider is a cloud–shock interaction problem which involves strong MHD shocks interacting with a dense cloud. We take the same initial data as in [26, 27]. The computational domain, $\Omega = [0, 2] \times [0, 1]$, is divided into three regions initially: the post-shock region $\Omega_1 = \{(x, y): 0 \leq x \leq 1.2, 0 \leq y \leq 1\}$, the pre-shock region $\Omega_2 = \{(x, y): 1.2 \leq x \leq 2, 0 \leq y \leq 1, \sqrt{(x - 1.4)^2 + (y - 0.5)^2} \geq 0.18\}$ and the cloud region $\Omega_3 = \{(x, y): \sqrt{(x - 1.4)^2 + (y - 0.5)^2} < 0.18\}$. The initial data in Ω_1 , Ω_2 and Ω_3 for $(\rho, u_x, u_y, u_z, B_x, B_y, B_z, p)$ is given by $\mathbf{U}_1, \mathbf{U}_2$ and \mathbf{U}_3 , respectively, with

$$\begin{aligned} \mathbf{U}_1 &= (3.88968, 0, 0, -0.05234, 1, 0, 3.9353, 14.2641), \\ \mathbf{U}_2 &= (1, -3.3156, 0, 0, 1, 0, 1, 0.04), \\ \mathbf{U}_3 &= (5, -3.3156, 0, 0, 1, 0, 1, 0.04). \end{aligned}$$

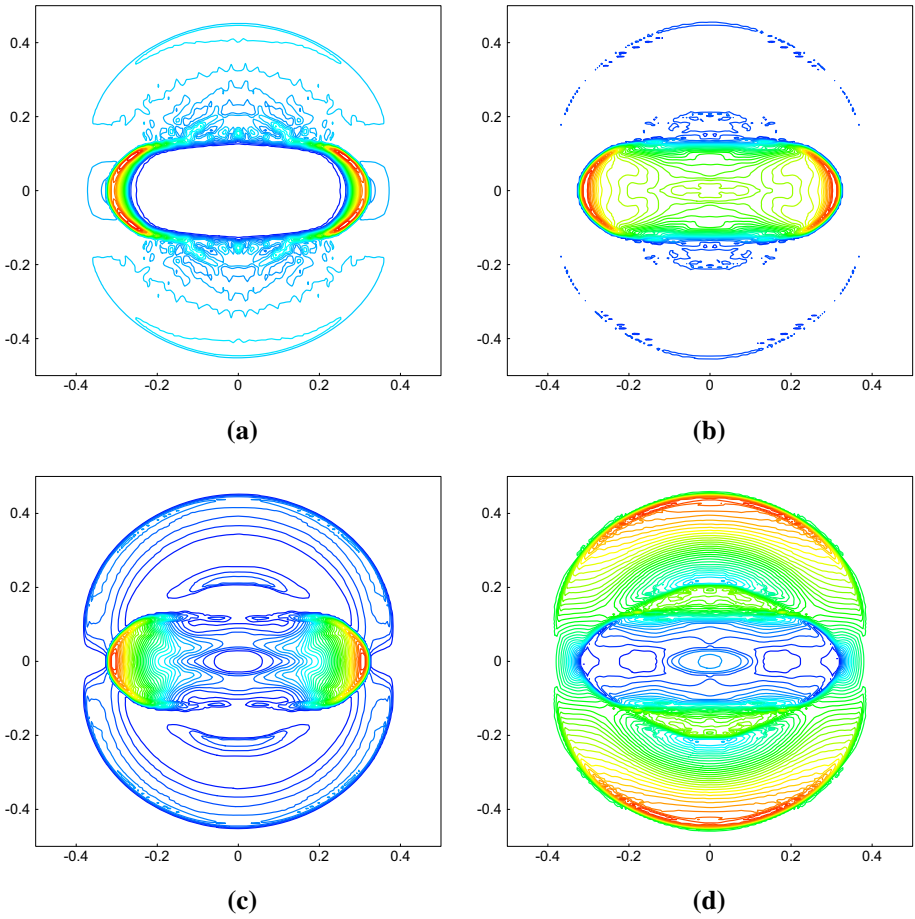


Fig. 12 P^2 approximation for the blast problem on the 200×200 mesh at $t = 0.01$. 40 equally spaced contours are plotted. **a** $\rho \in [0.191, 4.769]$, **b** $p \in [-16.397, 256.291]$, **c** $u_x^2 + u_y^2 \in [0, 288.838]$, **d** $B_x^2 + B_y^2 \in [426.407, 1236.830]$

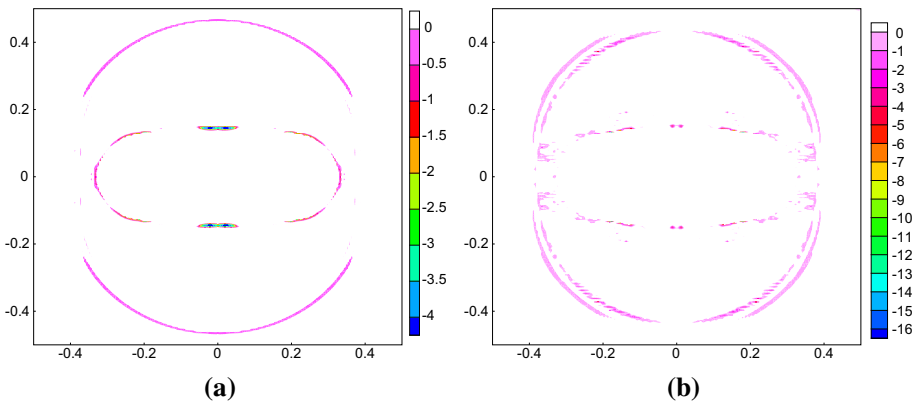


Fig. 13 Negative part of the pressure, $\min(0, p)$, in the blast problem with P^1 and P^2 approximations at $t = 0.01$ on the 200×200 mesh. **a** P^1 , **b** P^2

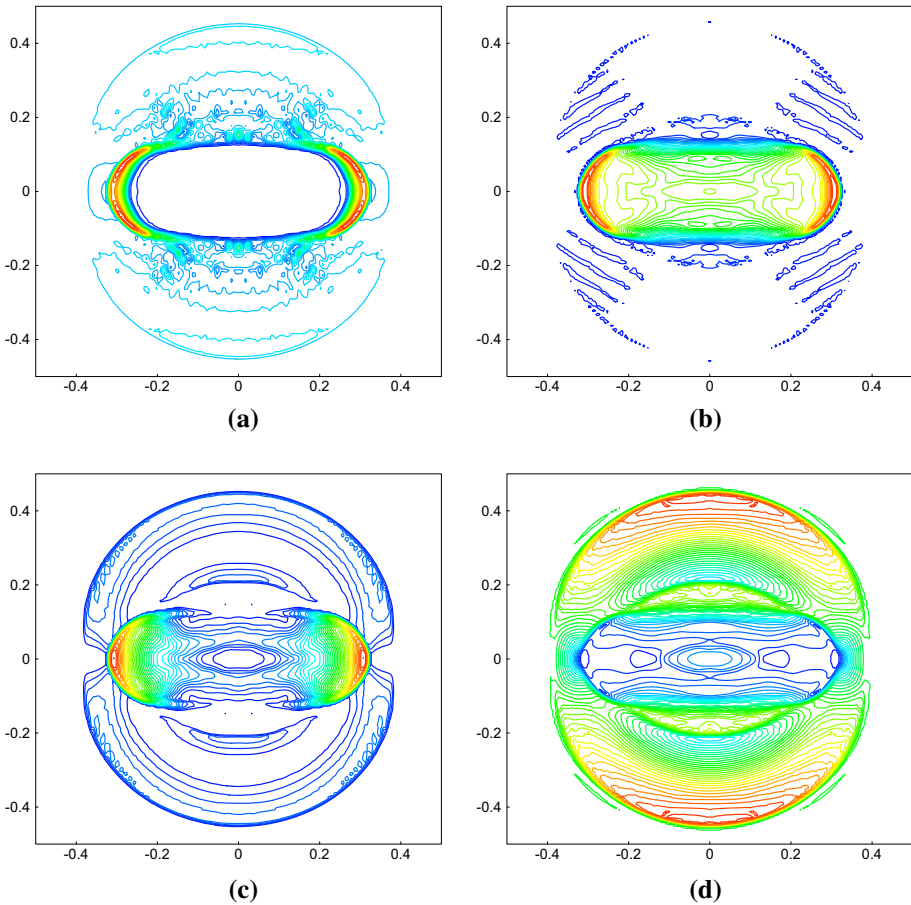


Fig. 14 P^2 approximation for the blast problem on the 200×200 mesh at $t = 0.01$. Nonlinear limiter is applied to both \mathbf{U}_h and $\{b_{ij}^x\}_{ij}, \{b_{ij}^y\}_{ij}$. 40 equally spaced contours are used. **a** $\rho \in [0.182, 4.573]$, **b** $p \in [-7.347, 254.906]$, **c** $u_x^2 + u_y^2 \in [0, 287.389]$, **d** $B_x^2 + B_y^2 \in [422.866, 1188.86]$

The cloud in the region Ω_3 is five times denser than its surrounding. Outgoing boundary conditions are used and $\gamma = 5/3$. We run the simulation up to $t = 0.6$.

In Fig. 15, we show the gray-scale images of the P^1 approximations for density ρ , pressure p and magnetic field component B_x, B_y on the 600×300 mesh. The white area represents relatively larger value. The numerical results are fairly close to those by exactly divergence-free central DG methods in [26, 27]. The *minmod* TVB limiter is implemented in the local characteristic fields and is only applied to \mathbf{U}_h .

In Fig. 16, gray-scale images of P^2 approximations are shown for density ρ , pressure p and magnetic field component B_x, B_y on the 600×300 mesh. In Fig. 17, we further plot the cut lines of density ρ based on P^2 approximation with $y = 0.6$ and $x = 1.0$ on the 600×300 and 800×400 meshes. The convergence of the methods is confirmed. With P^2 approximation, it is not sufficient to just apply the nonlinear limiter to \mathbf{U}_h for numerical stability. And the results presented here are obtained when the limiter is applied to both \mathbf{U}_h and $\{b_{ij}^x\}_{ij}, \{b_{ij}^y\}_{ij}$. In order to see the necessity to limit the magnetic field is related to the

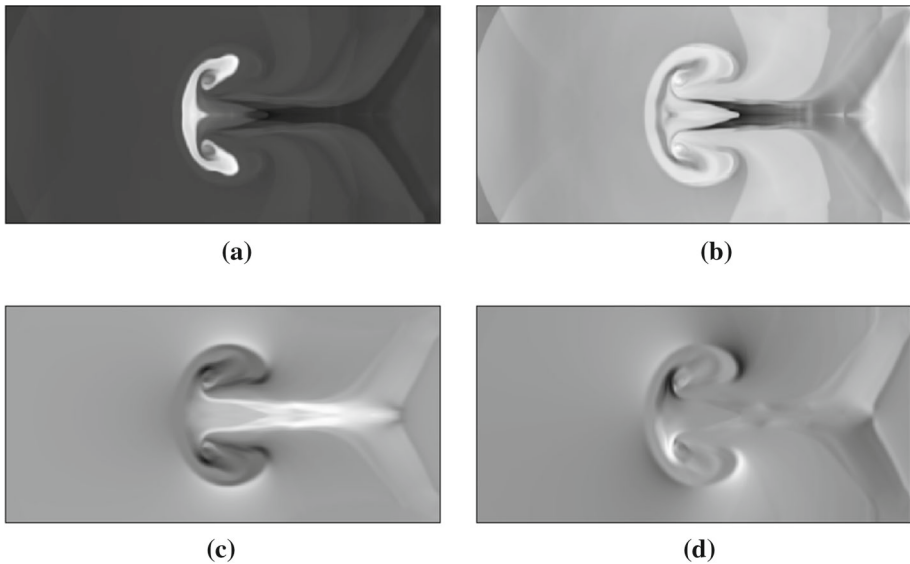


Fig. 15 P^1 approximation of the cloud–shock interaction problem at $t = 0.6$ on the 600×300 mesh. **a** $\rho \in [1.804, 11.638]$, **b** $p \in [6.295, 15.567]$, **c** $B_x \in [-3.073, 4.355]$, **d** $B_y \in [-3.299, 3.265]$

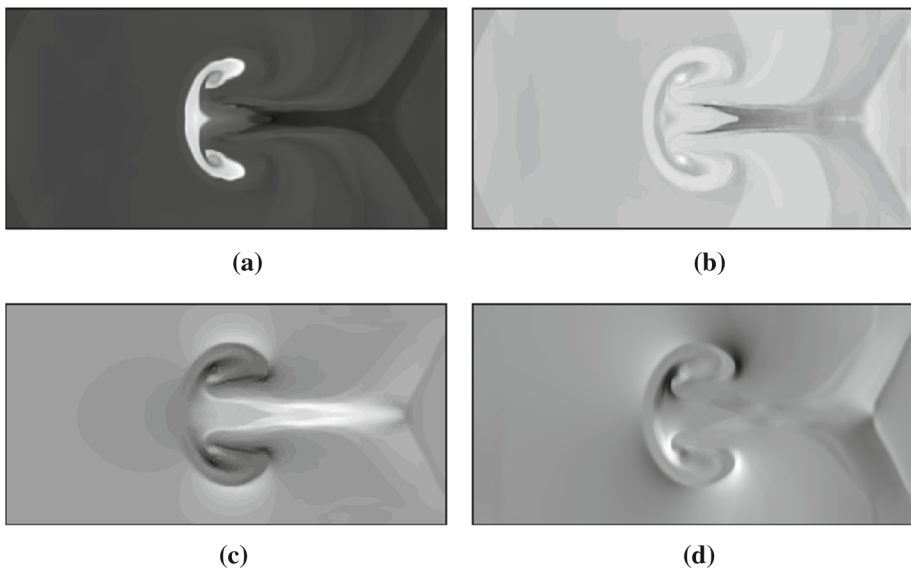


Fig. 16 P^2 approximation of the cloud–shock interaction problem at $t = 0.6$ on the 600×300 mesh. **a** $\rho \in [1.777, 11.655]$, **b** $p \in [1.028, 16.734]$, **c** $B_x \in [-2.922, 4.472]$, **d** $B_y \in [-3.027, 2.961]$

strength of the discontinuity, we also simulate a similar clock–shock interaction example, with the cloud in region Ω_3 two times denser than its surrounding at $t = 0$. As expected, our methods are stable for this modified example when the limiter is applied only to \mathbf{U}_h . The numerical results are not included here.

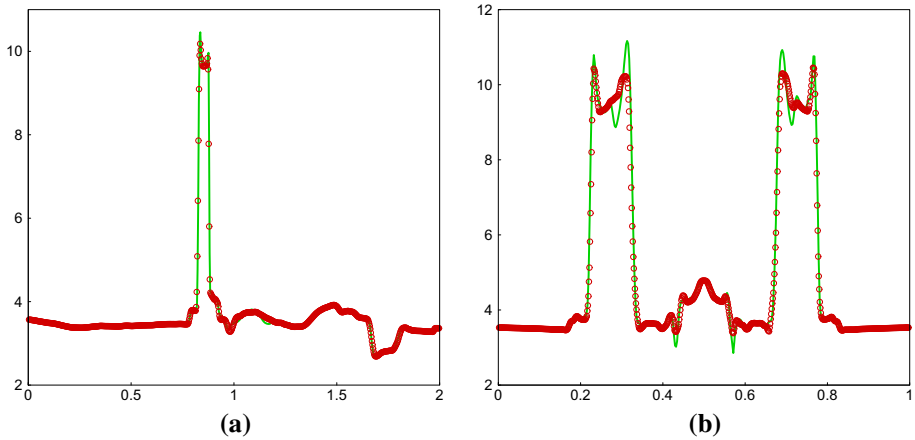


Fig. 17 The P^2 approximation of ρ in the cloud–shock interaction problem at $t = 0.6$ on 600×300 (circle) and 800×400 (solid) meshes. **a** $y = 0.6$, **b** $x = 1.0$

7 Concluding Remarks

In this paper, we propose second and third order globally divergence-free discontinuous Galerkin methods for ideal MHD equations on structured meshes in two dimensions. The main technical aspect is on the choices of numerical fluxes used in the different parts of the algorithms. Analysis is presented to identify conditions on numerical fluxes to ensure the exactly divergence-free property of the approximated magnetic field. A careful numerical and analytical study was carried out to find good choices of numerical fluxes for the accuracy and numerical stability of the methods. A set of smooth and non-smooth numerical examples are presented to illustrate the performance of the proposed methods. Our future efforts will include the extension of the methods to high order accuracy, three dimensions, and unstructured meshes.

References

1. Balsara, D.S.: Divergence-free adaptive mesh refinement for magnetohydrodynamics. *J. Comput. Phys.* **174**(2), 614–648 (2001)
2. Balsara, D.S.: Second-order-accurate schemes for magnetohydrodynamics with divergence-free reconstruction. *Astrophys. J. Suppl. Ser.* **151**(1), 149–184 (2004)
3. Balsara, D.S.: Divergence-free reconstruction of magnetic fields and WENO schemes for magnetohydrodynamics. *J. Comput. Phys.* **228**(14), 5040–5056 (2009)
4. Balsara, D.S.: Multidimensional HLLC Riemann solver: application to Euler and magnetohydrodynamic flows. *J. Comput. Phys.* **229**(6), 1970–1993 (2010)
5. Balsara, D.S., Dumbser, M.: Divergence-free MHD on unstructured meshes using high order finite volume schemes based on multidimensional Riemann solvers. *J. Comput. Phys.* **299**, 687–715 (2015)
6. Balsara, D.S., Dumbser, M., Abgrall, R.: Multidimensional HLLC Riemann solver for unstructured meshes with application to Euler and MHD flows. *J. Comput. Phys.* **261**, 172–208 (2014)
7. Balsara, D.S., Käppeli, R.: Von Neumann stability analysis of globally divergence-free RKDG schemes for the induction equation using multidimensional Riemann solvers. *J. Comput. Phys.* **336**, 104–127 (2017)
8. Balsara, D.S., Spicer, D.S.: A staggered mesh algorithm using high order Godunov fluxes to ensure solenoidal magnetic fields in magnetohydrodynamic simulations. *J. Comput. Phys.* **149**(2), 270–292 (1999)

9. Brackbill, J., Barnes, D.: The effect of nonzero $\nabla \cdot \mathbf{B}$ on the numerical solution of the magnetohydrodynamic equations. *J. Comput. Phys.* **35**(3), 426–430 (1980)
10. Brezzi, F., Douglas, J., Marini, L.D.: Two families of mixed finite elements for second order elliptic problems. *Numer. Math.* **47**(2), 217–235 (1985)
11. Brezzi, F., Fortin, M., Marini, L.D., et al.: Efficient rectangular mixed finite elements in two and three space variables. *ESAIM Math. Model. Numer. Anal.* **21**(4), 581–604 (1987)
12. Cheng, Y., Li, F., Qiu, J., Xu, L.: Positivity-preserving DG and central DG methods for ideal MHD equations. *J. Comput. Phys.* **238**, 255–280 (2013)
13. Cockburn, B., Hou, S., Shu, C.-W.: The Runge-Kutta local projection discontinuous Galerkin finite element method for conservation laws. IV. The multidimensional case. *Math. Comput.* **54**(190), 545–581 (1990)
14. Cockburn, B., Lin, S.-Y., Shu, C.-W.: TVB Runge–Kutta local projection discontinuous Galerkin finite element method for conservation laws III: one-dimensional systems. *J. Comput. Phys.* **84**(1), 90–113 (1989)
15. Cockburn, B., Shu, C.-W.: TVB Runge–Kutta local projection discontinuous Galerkin finite element method for conservation laws. II. General framework. *Math. Comput.* **52**(186), 411–435 (1989)
16. Cockburn, B., Shu, C.-W.: The Runge–Kutta discontinuous Galerkin method for conservation laws V: multidimensional systems. *J. Comput. Phys.* **141**(2), 199–224 (1998)
17. Dai, W., Woodward, P.R.: A simple finite difference scheme for multidimensional magnetohydrodynamical equations. *J. Comput. Phys.* **142**(2), 331–369 (1998)
18. Dedner, A., Kemm, F., Kröner, D., Munz, C.D., Schnitzer, T., Wesenberg, M.: Hyperbolic divergence cleaning for the MHD equations. *J. Comput. Phys.* **175**(2), 645–673 (2002)
19. Evans, C.R., Hawley, J.F.: Simulation of magnetohydrodynamic flows: a constrained transport method. *Astrophys. J.* **332**, 659–677 (1988)
20. Gardiner, T.A., Stone, J.M.: An unsplit Godunov method for ideal MHD via constrained transport. *J. Comput. Phys.* **205**(2), 509–539 (2005)
21. Gottlieb, S., Shu, C.-W., Tadmor, E.: Strong stability-preserving high-order time discretization methods. *SIAM Rev.* **43**(1), 89–112 (2001)
22. Hesthaven, J.S., Warburton, T.: *Nodal Discontinuous Galerkin Methods: Algorithms, Analysis, and Applications*. Springer, Berlin (2007)
23. Jiang, G.-S., Wu, C.: A high-order WENO finite difference scheme for the equations of ideal magnetohydrodynamics. *J. Comput. Phys.* **150**(2), 561–594 (1999)
24. Li, B.Q.: *Discontinuous Finite Elements in Fluid Dynamics and Heat Transfer*. Springer, Berlin (2005)
25. Li, F., Shu, C.-W.: Locally divergence-free discontinuous Galerkin methods for MHD equations. *J. Sci. Comput.* **22**(1), 413–442 (2005)
26. Li, F., Xu, L.: Arbitrary order exactly divergence-free central discontinuous Galerkin methods for ideal MHD equations. *J. Comput. Phys.* **231**(6), 2655–2675 (2012)
27. Li, F., Xu, L., Yakovlev, S.: Central discontinuous Galerkin methods for ideal MHD equations with the exactly divergence-free magnetic field. *J. Comput. Phys.* **230**(12), 4828–4847 (2011)
28. Li, S.: High order central scheme on overlapping cells for magneto-hydrodynamic flows with and without constrained transport method. *J. Comput. Phys.* **227**(15), 7368–7393 (2008)
29. Li, S.: A fourth-order divergence-free method for MHD flows. *J. Comput. Phys.* **229**(20), 7893–7910 (2010)
30. Powell, K.G.: An Approximate Riemann Solver for Magnetohydrodynamics (that works in more than one dimension). ICASE report No. 94-24, Langley (1994)
31. Qiu, J., Shu, C.-W.: Runge–Kutta discontinuous Galerkin method using WENO limiters. *SIAM J. Sci. Comput.* **26**(3), 907–929 (2005)
32. Raviart, P.A., Thomas, J.M.: A mixed finite element method for 2-nd order elliptic problems. In: Dold, A., Eckmann, B. (eds.) *Mathematical Aspects of Finite Element Methods*. Proceedings of the Conference Held in Rome, 10-12 Dec, 1975. Lecture Notes in Mathematics, vol. 606 (1977). Springer, Berlin, Heidelberg (1977)
33. Reed, W. H., Hill, T. R.: *Triangular Mesh Methods for the Neutron Transport Equation*, Technical Report LA-UR-73-479. Los Alamos Scientific Laboratory (1973)
34. Riviere, B.: *Discontinuous Galerkin Methods for Solving Elliptic and Parabolic Equations: Theory and Implementation*. SIAM, Philadelphia (2008)
35. Rossmannith, J. A.: High-order discontinuous Galerkin finite element methods with globally divergence-free constrained transport for ideal MHD. arXiv preprint [arXiv:1310.4251](https://arxiv.org/abs/1310.4251), (2013)
36. Shu, C.-W.: TVB uniformly high-order schemes for conservation laws. *Math. Comput.* **49**(179), 105–121 (1987)

37. Tóth, G.: The $\nabla \cdot \mathbf{B}$ constraint in shock-capturing magnetohydrodynamics codes. *J. Comput. Phys.* **161**(2), 605–652 (2000)
38. Yakovlev, S., Xu, L., Li, F.: Locally divergence-free central discontinuous Galerkin methods for ideal MHD equations. *J. Comput. Sci.* **4**(1), 80–91 (2013)
39. Yang, H., Li, F.: Stability analysis and error estimates of an exactly divergence-free method for the magnetic induction equations. *ESAIM Math. Model. Numer. Anal.* **50**(4), 965–993 (2016)
40. Yee, K.S.: Numerical solution of initial boundary value problems involving Maxwell's equations in isotropic media. *IEEE Trans. Antennas Propag.* **14**(3), 302–307 (1966)
41. Zhang, X., Shu, C.-W.: On positivity-preserving high order discontinuous Galerkin schemes for compressible Euler equations on rectangular meshes. *J. Comput. Phys.* **229**(23), 8918–8934 (2010)